Chapter 4

Tracing the cold and warm physico-chemical structure of deeply embedded protostars

IRAS 16293-2422 versus VLA 1623-2417

Murillo, N. M., van Dishoeck, E. F., van der Wiel, M. H. D., Jørgensen, J. K., Drozdovskaya, M. N., Calcutt, H., Harsono, D.
submitted to A&A

Abstract

Context Much attention has been placed on the dust distribution in protostellar envelopes, but there are still many unanswered questions regarding the physico-chemical structure of the gas..

Aims Our aim is to start identifying the factors that determine the chemical structure of protostellar regions, by studying and comparing low-mass embedded systems in key molecular tracers.

Methods The cold and warm chemical structures of two embedded Class 0 systems, IRAS 16293-2422 and VLA 1623-2417, are characterized through interferometric observations. DCO^+, N_2H^+ and N_2D^+ are used to trace the spatial distribution and physics of the cold regions of the envelope, while c$-C_3H_2$ and C_2H are expected to trace the warm (UV-irradiated) regions.

Results The two sources show a number of striking similarities and differences. DCO^+ consistently traces the cold material at the disk-envelope interface, where gas temperatures are lowered due to disk shadowing. N_2H^+ and N_2D^+, also tracing cold gas, show low abundances towards VLA 1623-2417, but for IRAS 16293-2422, the distribution of N_2D^+ is consistent with the same chemical models that reproduce DCO^+. c$-C_3H_2$ and C_2H show different spatial distributions for the two systems, sometimes tracing the outflow cavity walls and in other cases the more quiescent envelope. In IRAS 1623-2422, c$-C_3H_2$ and C_2H are surprisingly anti-correlated.

Finally, hot core molecules are abundantly seen toward IRAS 16293-2422 but not toward VLA 1623-2417.

Conclusions We identify temperature as one of the key factors in determining the chemical structure of protostars as seen in gaseous molecules. More luminous protostars, such as IRAS 16293-2422, will have chemical complexity out to larger distances than colder protostars, such as VLA 1623-2417. Additionally, disks in the embedded phase have a crucial role in controlling both the gas and dust temperature of the envelope, and consequently the chemical structure.

4.1 Introduction

While there is a well-established outline of the physical evolution of protostellar systems (Evans 1999; Dunham et al. 2014; Li et al. 2014; Reipurth et al. 2014), there are still many questions regarding the physico-chemical structure of these systems. Several studies point out the chemical richness and diversity of young embedded protostars, most notably in the Class 0 stage, ranging from simple molecules to carbon chains and complex organics (see reviews by Herbst & van Dishoeck 2009; Caselli & Ceccarelli 2012; Sakai & Yamamoto 2013). In contrast, some other protostellar systems show much less chemical complexity (e.g., Jørgensen et al. 2005b; Maret et al. 2006; Öberg et al. 2014; Fayolle et al. 2015; Lindberg et al. 2014b, 2016, 2017; Bergner et al. 2017), a situation made more extreme when some starless cores have stronger molecular line emissions than the already formed protostars (e.g., Bergman et al. 2011; Bacmann et al. 2012; Friesen et al. 2014). It is interesting to explore the chemical structure and evolution of early stage protostars and what physical quantities dictate the resulting chemical structure as observed in the gas phase.

The chemical fingerprint generated in the early embedded stages of star formation may be transmitted to the later stages and eventually the protoplanetary disk, where planets and comets are formed (e.g., Aikawa et al. 1999; Aikawa & Herbst 1999; Visser et al. 2009, 2011; Hincelin et al. 2013; Drozdovskaya et al. 2014; Willacy et al. 2015; Yoneda et al. 2016). Which factors then generate a protostellar system's fingerprint? Protostellar cores may inherit their chemical composition from the parent cloud that eventually collapses to form protostars (e.g., Aikawa et al. 2012; Furuya et al. 2012; Tassis et al. 2012; Hincelin et al. 2016). It would then seem likely that protostars from the same parent cloud would have a similar chemical composition. However, this would require the cloud to have a homogeneous composition, which is not always the case (Bergman et al. 2011). Instead, other mechanisms could alter the chemical fingerprint. Turbulence and large-scale motions could stir the core around, moving material from the outer region of the core closer to the warmer regions of the system, kick-starting chemical reactions and producing enhancements of selected species. Formation of more complex chemical species likely occurs through solid-phase reactions (i.e., on ice and dust surfaces) instead of in the gas-phase, and such reactions proceed faster at higher dust temperatures which increases the mobility of radicals (Garrod & Herbst 2006). If material near outflow cavities is warmer than elsewhere in the envelope, this could generate pockets of chemically rich ices that, once heated above the sublimation temperature, would be released into the gas-phase (Drozdovskaya et al. 2015). Moreover, UV radiation can photodissociate CO and create free atomic carbon that leads to efficient formation of carbon-bearing molecules. UV irradiation together with age and variations in accretion rates would also produce different outcomes, even

with the same initial ingredients. In addition, simple warm-chemistry molecules can be the precursors to more complex molecules (Sakai & Yamamoto 2013).

The physical evolution of the individual protostars, e.g., the collapse time and structure, will also impact the chemical fingerprint. An important consideration regarding the physical structure is that disks may have formed already in the early stages, as shown by recent observations (e.g., Tobin et al. 2012b; Murillo et al. 2013; Harsono et al. 2014; Lindberg et al. 2014a; Codella et al. 2014; Yen et al. 2017). Not only do disks provide a high density long-lived reservoir preventing molecules from falling into the star, but they also affect the thermal structure of their surroundings. Thus the disk-envelope interface and the envelope itself must be studied (Murillo et al. 2015; Persson et al. 2016). The disk-envelope interface and the outer envelope of embedded systems are traced by cold-chemistry molecules, since these regions are usually shielded from heating by the central protostar (van Dishoeck et al. 1995; Jørgensen et al. 2004, 2005a; Sakai et al. 2014c; Murillo et al. 2015). Through the study of molecules sensitive to temperature, we can then understand the structure of embedded protostellar systems.

Aiming to explore the chemical evolution of the earliest embedded protostellar systems, i.e. Class 0, we compare two systems from ρ Ophiuchus ($d \sim 120$ pc, Loinard et al. 2008), IRAS 16293-2422 and VLA 1623-2417, separated by a projected distance of 2.8 pc. Most previous studies were based on single-dish studies. The advent of Atacama Large Millimeter/submillimeter Array (ALMA) now allows chemical studies on 100 AU scales that spatially resolve the different physical components of the system.

IRAS 16293-2422 (hereafter IRAS in the text) is a widely studied multiple system, located in L1689N, with a complicated outflow structure being driven by source A (Stark et al. 2004; Yeh et al. 2008; Loinard et al. 2013). IRAS-A and B, separated by about 620 AU, have different inclination angles, with A's disk-like structure being inclined and B orientated face-on with respect to the line of sight (Pineda et al. 2012; Jørgensen et al. 2016). Due to the different inclination angles, it is difficult to determine whether these systems are at the same evolutionary stage or not (Murillo et al. 2016, see chapter 5). Both components are chemically rich but show differences in structure (Bottinelli et al. 2004; Bisschop et al. 2008; Jørgensen et al. 2011).

VLA 1623-2417 (hereafter VLA in the text) is a triple protostellar system, located in L1688 (ρ Oph A), mostly studied for its prominent outflow in the region (André et al. 1990; Caratti o Garatti et al. 2006). The three components of the system, VLA-A, B and W are separated by 132 and 1200 AU, respectively, have similar inclination angles, and have also been found to be at different evolutionary stages (Murillo & Lai 2013; Murillo et al. 2013, see chapter 2). VLA has been shown to be largely line poor in single-dish studies (Garay et al. 2002; Jørgensen et al. 2004; Bergman et al. 2011; Friesen et al. 2014).

In this paper, we present observations of DCO^+, N_2H^+, N_2D^+, c$-C_3H_2$ and C_2H towards IRAS and VLA, using the ALMA, the Submillimeter Array (SMA) and the Atacama Pathfinder EXperiment (APEX), details of which are described in Sect. 4.2. DCO^+, N_2H^+ and N_2D^+ are known to be good tracers of cold gas where CO is frozen out. c$-C_3H_2$ and C_2H are usually seen in photon-dominated regions (PDRs) such as the Orion Bar (Pety et al. 2007; van der Wiel et al. 2009; Nagy et al. 2015) and the Horsehead Nebula (Cuadrado et al. 2015; Guzmán et al. 2015), with both species located at the irradiated, and thus warmer, edge of these regions. c$-C_3H_2$ and C_2H could thus be expected to trace the (UV-irradiated) outflow cavity walls, although

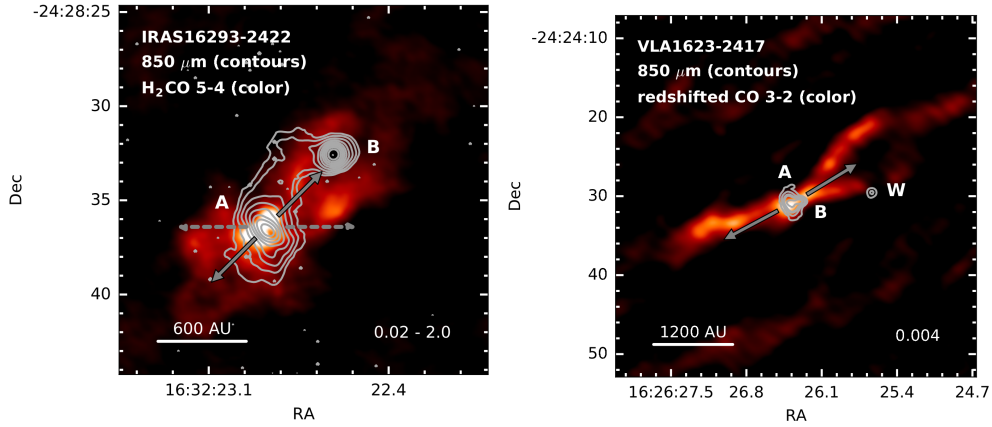

Figure 1: Continuum at 850μm (contours) for both systems, IRAS 16293-2422 (left) and VLA 1623-2417 (right), overlaid on H_2CO and redshifted CO (color-scale), respectively. For VLA 1623-2417, contours are in steps of 3, 8, 15, 20 and 50σ, with σ = 0.004 Jy beam^{-1}. For IRAS 16293-2422, the levels are logarithmically spaced between 0.02 and 2 Jy beam^{-1}, and highlight the ridge that spans between sources A and B. The arrows show the direction of red- and blue-shifted outflows from source A in each system.

both species have also been found just outside the disk-envelope interface (Sakai et al. 2014b). Besides mapping their distributions, multiple lines from a single molecule can also be used to trace physical conditions such as temperature and density (van Dishoeck et al. 1993; Evans 1999; van der Tak et al. 2007; Shirley 2015) and the current dataset allows this to be done for several species.

Section 4.3 describes the spatial distribution of each molecule for both systems. The observations are compared to chemical models and physical parameters are derived in Sect. 4.4. Sections 4.5 and 4.6 compare both systems studied here with other objects found in literature and place the results of our work in context.

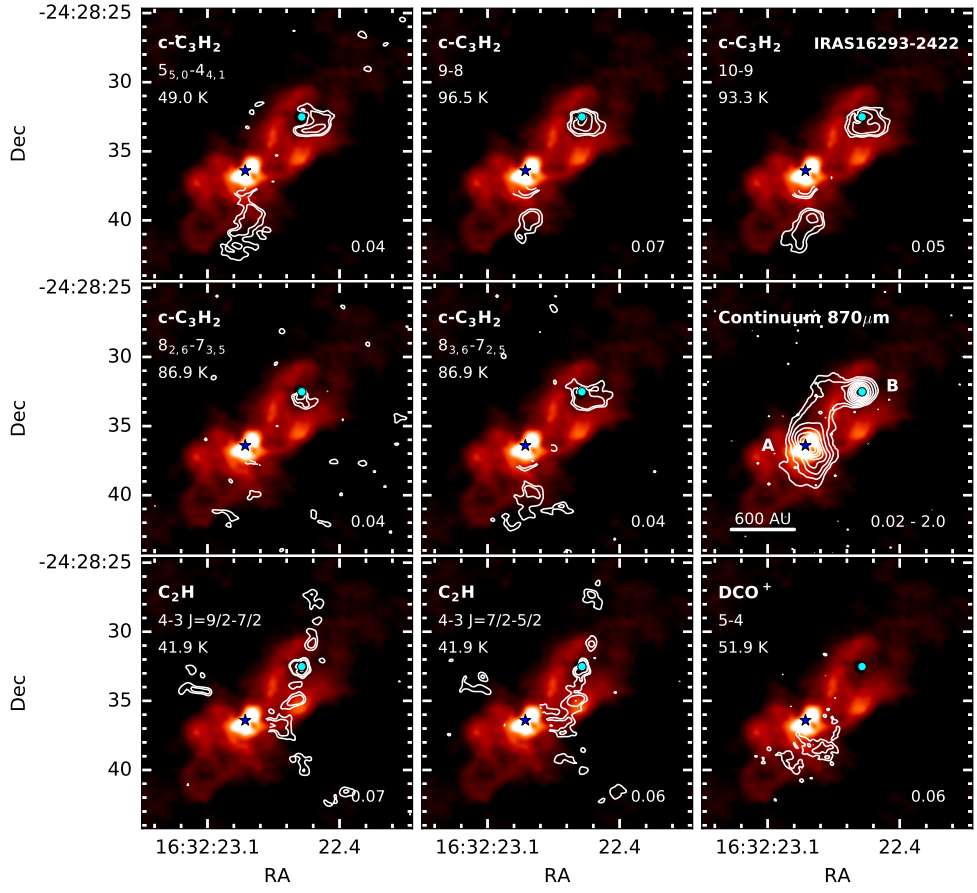

Figure 2: Intensity integrated maps (contours) of c$-C_3H_2$, C_2H, DCO^+ and continuum towards IRAS 16293-2422. H_2CO 5–4 is shown in color-scale. Contours show the respective lines in steps of 2, 3, 5, 20 and 60σ, with σ (Jy beam^{-1} km s^{-1}) indicated in the lower right of each panel. For continuum, the levels are logarithmically spaced between 0.02 and 2 Jy beam^{-1}, and highlight the ridge that spans between sources A and B. The positions of IRAS 16293-2422 A and B are indicated with a star and circle, respectively. For the c$-C_3H_2$ and C_2H panels, the emission centered on A is contamination from other molecule(s) and is masked out in a radius of 2″ from the position of A.

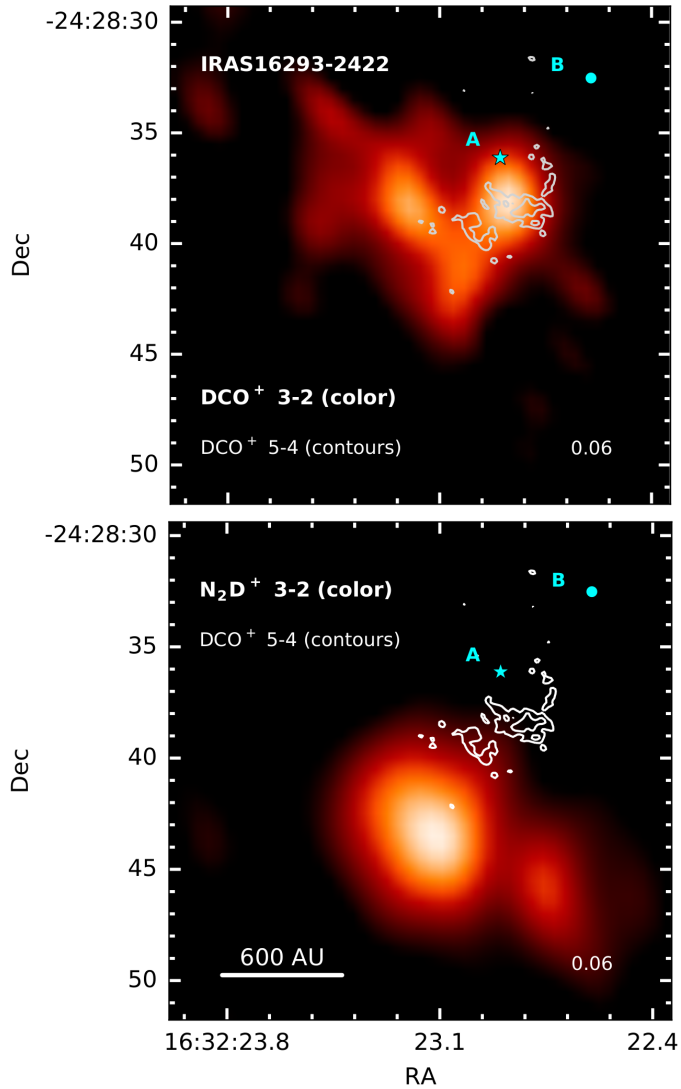

Figure 3: Intensity integrated maps of DCO^+ 3–2 (top) and N_2D^+ 3–2 (bottom) observed with the SMA, overlaid with DCO^+ 5–4 (contours) observed with ALMA. Contours are the same as in Fig. 2. The positions of IRAS 16293-2422 A and B are indicated with a star and circle, respectively. Both DCO^+ transitions match spatially, and N_2D^+ is located beyond the extent of the DCO^+ emission. Note the different center of this figure compared to Fig. 2.

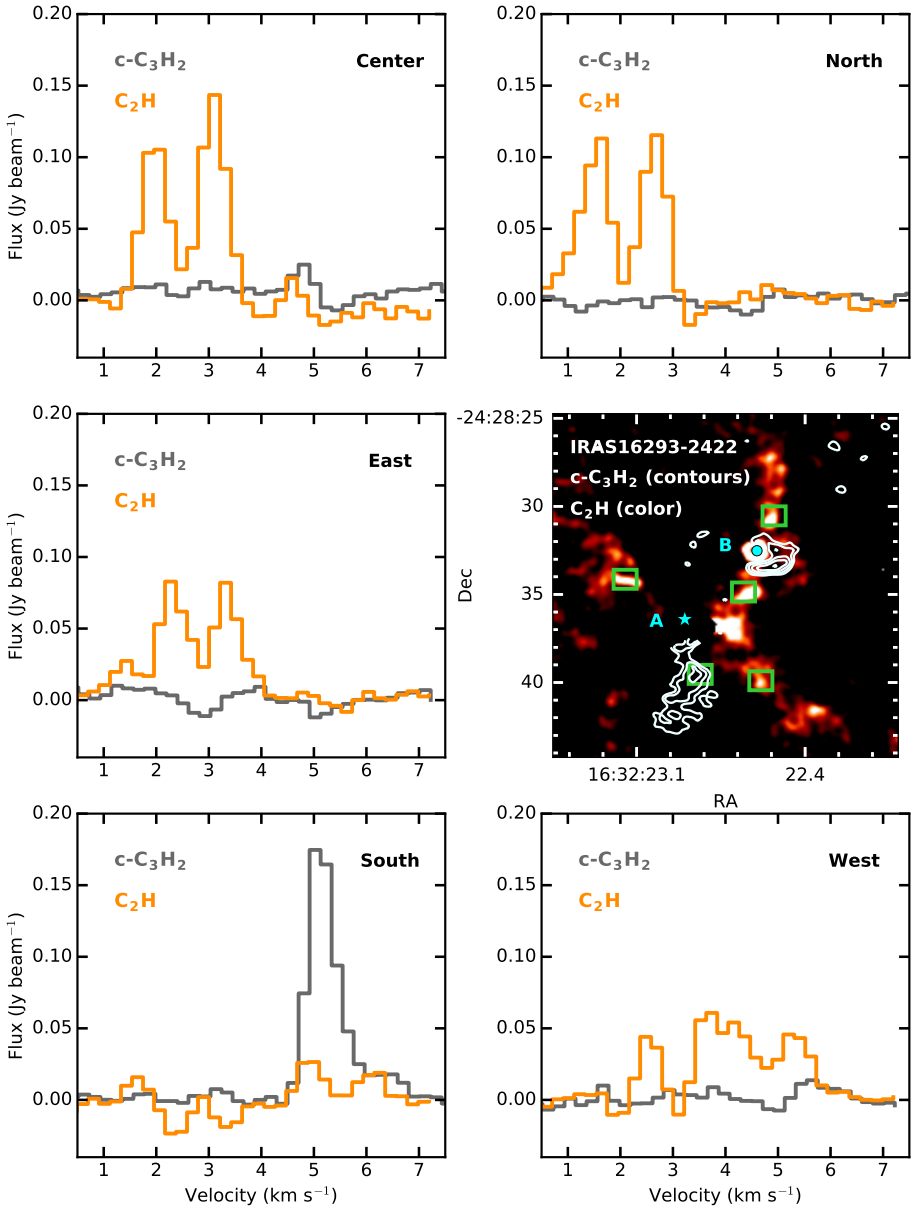

Figure 4: IRAS 16293-2422 c$-C_3H_2$ 5–4 and C_2H 4–3 J=9/2–7/2 spectra taken at 5 positions, indicated by the green boxes in the intensity integrated map presented in the left bottom panel. The anti-correlation of both molecules is seen at all positions. The region within a radius of 2″ from the position of source A is contaminated by other molecular species, and is masked out for these maps.

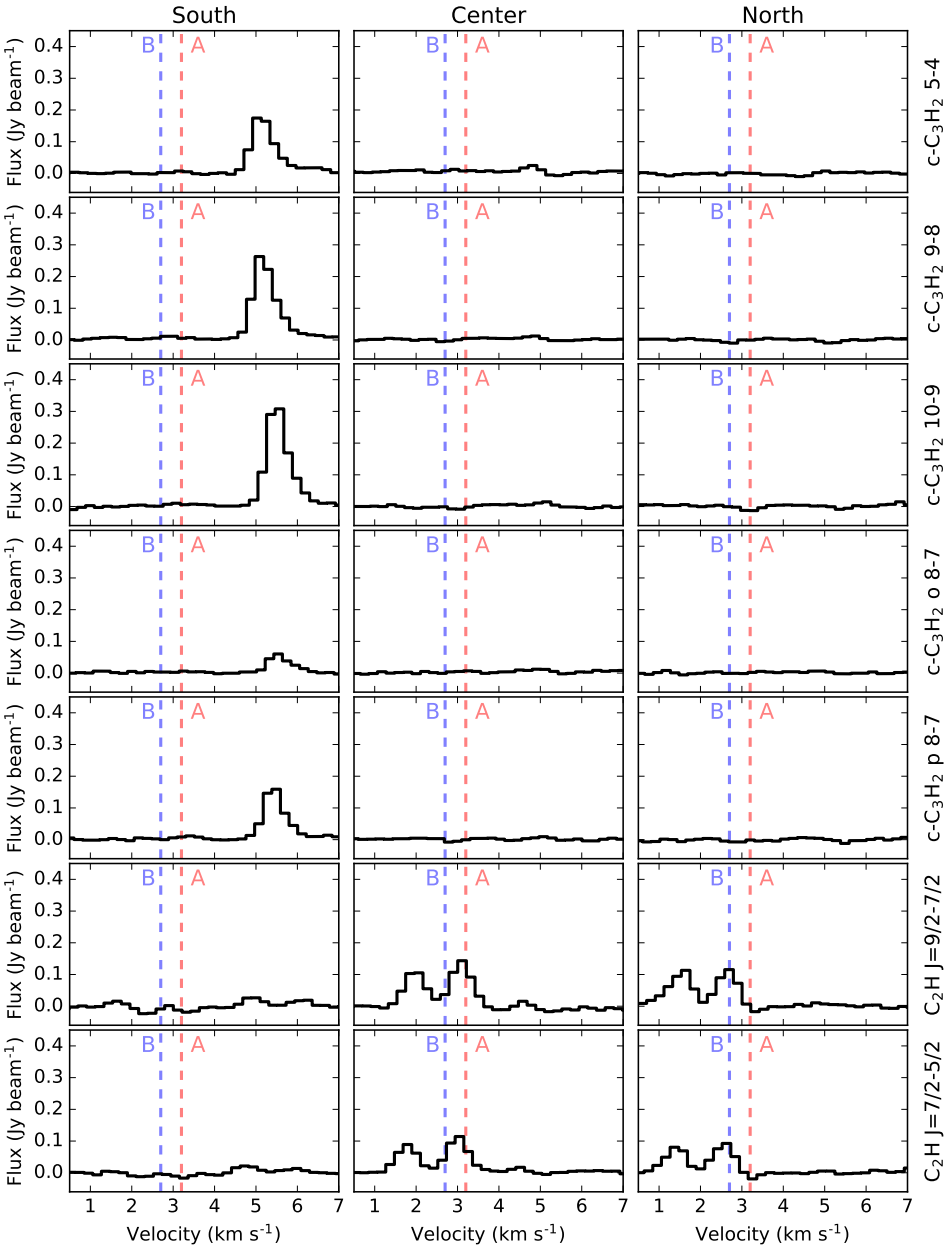

Figure 5: IRAS 16293-2422 ALMA spectra for all transitions of c−C_3H_2 and C_2H for each of the south, center and north positions shown in Fig. 4. The systemic velocities of sources A and B are marked with the vertical dashed lines. The anti-correlation of c−C_3H_2 and C_2H is also evident in the spectra shown here.

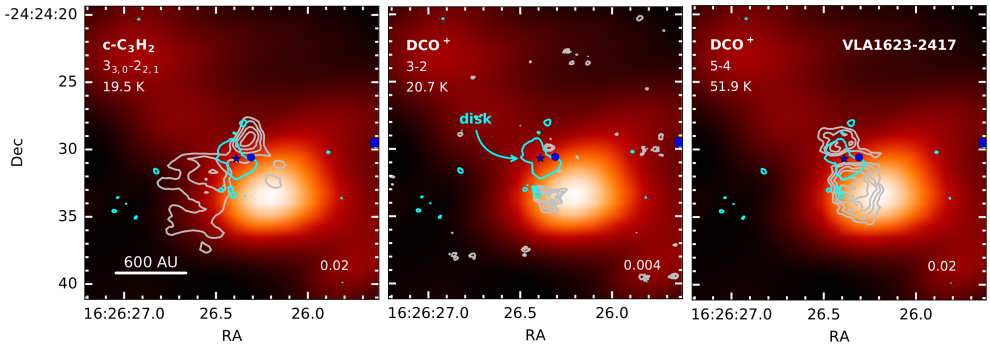

Figure 6: Intensity integrated maps (gray contours) of c$-C_3H_2$ and DCO^+ towards VLA 1623-2417. DCO^+ 3–2 from ACA observations is shown in color-scale. The cyan line is the 3σ contour of $C^{18}O$ in order to show the location and extent of the rotating disk centered on VLA 1623-2417 A. Gray contours show the respective lines in steps of 3, 4, 5 and 6σ, except for DCO^+ 3–2 where the contours start at 4σ. The value of σ (Jy beam^{-1} km s^{-1}) is indicated in the lower right corner of each panel. The positions of VLA 1623-2417 A, B and W are indicated with a star, circle and square, respectively.

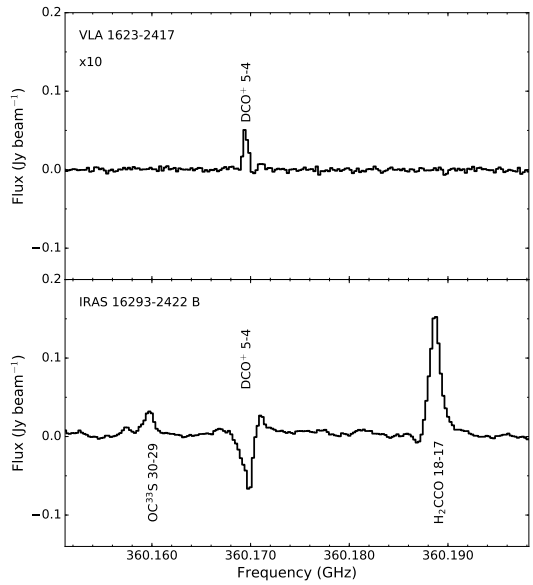

Figure 7: Comparison of the spectra centered on DCO^+ 5–4 of VLA 1623-2417 A and one beam offset from IRAS 16293-2422 B. The spectra for VLA 1623-2417 has been multiplied by a factor of 10 in order to compare more easily. Note the lack of molecular line emission toward VLA 1623-2417 in contrast to IRAS 16293-2422.

Table 1: Summary of line observations.

					IRAS 16293-2422		VLA 1623-2417	
Line	Transition	ν GHz	$\log_{10}$ A_{ij}	E_{up} K	Peak Flux mJy beam^{-1}	Line width km s^{-1}	Peak Flux mJy beam^{-1}	Line width km s^{-1}
				ALMA				
c$-C_3H_2$	$3_{3,0}$–$2_{2,1}$	216.27876	-3.33	19.46	...	...	190	0.5
c$-C_3H_2$	$5_{5,0}$–$4_{4,1}$	349.26400	-2.78	48.98	240[a]	1.0	...	...
c$-C_3H_2$	10–9[b]	351.78158	-2.61	96.49	410[a]	1.0	...	...
c$-C_3H_2$	9–8[c]	351.96597	-2.67	93.34	350[a]	1.0	...	...
c$-C_3H_2$	$8_{2,6}$–$7_{3,5}$	352.18554	-2.76	86.93	90[a]	1.0	...	...
c$-C_3H_2$	$8_{3,6}$–$7_{2,5}$	352.19364	-2.76	86.93	200[a]	1.0	...	...
C_2H	4–3 J=9/2–7/2 F=5–4	349.33771	-3.88	41.91	170	0.7	...	...
C_2H	4–3 J=9/2–7/2 F=4–3	349.33899	-3.89	41.91	140	0.7	...	...
C_2H	4–3 J=7/2–5/2 F=4–3	349.39927	-3.90	41.93	140	0.7	...	...
C_2H	4–3 J=7/2–5/2 F=3–2	349.40067	-3.92	41.93	110	0.7	...	...
DCO^+	3–2	216.11258	-2.62	20.74	...	...	90	0.7
DCO^+	5–4	360.16978	-2.42	51.86	10	1.0	290	0.7
N_2D^+	3–2	231.32166	-2.66	22.20	...	...	<8.58[d]	...
N_2H^+	4–3	372.67251	-2.51	44.71	...	...	<94.9[d]	...
				SMA				
DCO^+	3–2	216.11258	-2.62	20.74	1800	1.0	...	...
N_2D^+	3–2	231.32166	-2.66	22.20	1700	2.0	...	...

Table 1: continued.

					IRAS 16293-2422		VLA 1623-2417	
Line	Transition	ν	$\log_{10}$ A_{ij}	E_{up}	Peak Flux	Line width	Peak Flux	Line width
			APEX (T_{mb})					
C_2H	4–3 J=9/2–7/2 F=5–4	349.33771	-3.88	41.91	...	...	0.96 K	0.7
C_2H	4–3 J=9/2–7/2 F=4–3	349.33899	-3.89	41.91	...	...	0.62 K	0.7
C_2H	4–3 J=7/2–5/2 F=4–3	349.39927	-3.90	41.93	...	...	0.68 K	0.7
C_2H	4–3 J=7/2–5/2 F=3–2	349.40067	-3.92	41.93	...	...	0.34 K	0.7
DCO^+	3–2	216.11258	-2.62	20.74	...	...	4.8 K	0.8
DCO^+	5–4	360.16978	-2.42	51.86	...	...	2.2 K	0.8

Notes. [a] c$-C_3H_2$ peak fluxes and line widths taken from the south peak where there is no line confusion. [b] Blended $10_{0,10}$–$9_{1,9}$ and $10_{1,10}$–$9_{0,9}$ transitions of c$-C_3H_2$. [c] Blended $9_{1,8}$–$8_{2,7}$ and $9_{2,8}$–$8_{1,7}$ transitions of c$-C_3H_2$. [d] 1 σ noise level of N_2D^+ and N_2H^+ in 0.02 km s^{-1} channel

References. All rest frequencies were taken from the Cologne Database for Molecular Spectroscopy (CDMS) (Endres et al. 2016). The c$-C_3H_2$ entry was based on Bogey et al. (1987) with transition frequencies important for our survey from Bogey et al. (1986) and from Spezzano et al. (2012). The CCH entry is based on Padovani et al. (2009) with additional important data from Müller et al. (2000) and Sastry et al. (1981). The DCO^+ and N_2H^+ entries are based on Caselli & Dore (2005) and on Cazzoli et al. (2012), respectively. Information on the N_2D^+ rest frequency was taken from Pagani et al. (2009a).

4.2 Observations

4.2.1 IRAS 16293-2422

IRAS was targeted in the "Protostellar Interferometric Line Survey" (PILS) program (Project-ID: 2013.1.00278.S; PI: Jes K. Jørgensen; Jørgensen et al. 2016), an ALMA Cycle 2 unbiased spectral survey in Band 7, using both the 12m array and the Atacama Compact Array (ACA). The spectral set-up covers a frequency range from 329.147 GHz to 362.896 GHz, and provides a velocity resolution of 0.2 km s^{-1}. The pointing coordinate was α_{J2000} = 16:32:22.72; δ_{J2000} = −24:28:34.3, set to be equidistant from the two sources A and B at $v_{\rm lsr}$ = 3.2 and 2.7 km s^{-1}, respectively. The 12m array and the ACA observations were combined, producing a synthesized beam of 0.5″×0.5″. A detailed description of the observations and reduction is given in Jørgensen et al. (2016). Many complex molecules detected in this survey (e.g., Coutens et al. 2016; Jørgensen et al. 2016; Lykke et al. 2017) show relatively compact emission peaking close to the location of the two protostars. This work focuses on a few of the molecules detected in the spectral survey that show extended emission, namely DCO^+, c−C_3H_2 and C_2H. For c−C_3H_2 and C_2H the combined 12m array and ACA data cubes are used. For DCO^+, the combined data cube and the ACA data separately are considered. The typical RMS noise is about 7–10 mJy $beam^{-1}$ per 0.2 km s^{-1} channel, and the flux calibration uncertainty is ∼5% (Jørgensen et al. 2016). Transitions and line frequencies of the molecular species used in this work are listed in Table 1, as well as the peak fluxes and line widths.

Since the PILS survey did not cover lines of N_2D^+ 3–2 or DCO^+ 3–2, we include here the observations of these two molecules from a spectral line survey with the SMA (Jørgensen et al. 2011). A brief description of the observations is given here. The pointing coordinate was α_{J2000} = 16:32:22.91; δ_{J2000} = −24:28:35.5. For DCO^+ 3–2, the beam size is 5.5″× 3.2″, while for N_2D^+ 3–2 the beam size is 4.0″× 2.4″. The RMS noise is 0.24 Jy $beam^{-1}$ for a 0.56 km s^{-1} channel width for DCO^+, and 0.06 Jy $beam^{-1}$ for a channel width of 1.1 km s^{-1} for N_2D^+. Further details on the reduction and analysis are given in Jørgensen et al. (2011). These data are considered in order to directly compare the cold chemistry of IRAS with that of VLA. Additionally, two transitions of DCO^+ are needed to derive temperature and density from line ratios.

4.2.2 VLA 1623-2417

VLA was observed with ALMA in Cycle 0 using Band 6, with pointing coordinates α_{J2000} = 16:26:26.419; δ_{J2000} = 24:24:29.988. The spectral set-up was configured to observe DCO^+ 3–2 and N_2D^+ 3–2 together with $C^{18}O$ 2–1 and ^{12}CO 2–1, providing a velocity resolution of 0.0847 km s^{-1} and a synthesized beam size of 0.85″×0.65″. DCO^+ 3–2 data from the Cycle 0 obseravations were previously presented in Murillo et al. (2015, see chapter 3). The data reduction results of $C^{18}O$ and ^{12}CO can be found in Murillo et al. (2013, see chapter 2) and Santangelo et al. (2015).

ALMA Cycle 2 observations in Bands 6 and 7 were also carried out, with pointing coordinates α_{J2000} = 16:26:26.390; δ_{J2000} = −24:24:30.688. The Band 6 observations provided a spatial and spectral resolution of about 0.45″×0.25″ and 0.0211 km s^{-1}, respectively, with a typical RMS noise of about 7–9 mJy $beam^{-1}$ per 0.0211 km s^{-1} velocity channel. The spectral set-up covered DCO^+, $C^{18}O$ and ^{13}CO together with continuum and was observed in both the ACA and the 12m array. Band 6 ACA

Table 2: Tests of the temperature and density profiles of the two sources.

Test	IRAS 16293-2422 (Crimier et al. 2010)			VLA 1623-2417 (Jørgensen et al. 2002)		
	$T_{27\mathrm{AU}}$ K	$n_{27\mathrm{AU}}$ cm^{-3}	Note	$T_{4\mathrm{AU}}$ K	$n_{4\mathrm{AU}}$ cm^{-3}	Note
1	300.0	2.36×10^{9}	unchanged	250.0	1.62×10^{9}	unchanged
2	300.0	2.36×10^{10}	$n \times 10$	250.0	1.62×10^{10}	$n \times 10$
3	300.0	2.36×10^{8}	n / 10	250.0	1.62×10^{8}	n / 10
4	100.0	2.36×10^{9}	T / 3	166.7	1.62×10^{9}	T / 1.5

observations of DCO^+ were presented in Murillo et al. (2015, see chapter 3); $C^{18}O$ and ^{13}CO are treated elsewhere (Cheong et al. in prep.). Band 7 observations, with a spectral set-up covering N_2H^+ 5–4, DCO^+ 5–4 and H_2D^+ $1_{1,0}$–$1_{1,1}$ together with continuum with only the 12m array, provided a spectral and spatial resolution of 0.025 km s^{-1} and $0.87'' \times 0.54''$, respectively. Total observing time was 0.9 hr with a 46% duty cycle, using 34 antennas and a maximum baseline of 350 m. Data calibration was done with J1517-2422, J1625-2527 and Titan for bandpass, gain and flux calibration, respectively. DCO^+ was detected with a noise of 26 mJy beam^{-1} per 0.025 km s^{-1}. The system temperature was relatively high for the spectral windows containing N_2H^+ and H_2D^+, causing the noise to be of about 95 mJy beam^{-1} per 0.025 km s^{-1} velocity channel, despite flagging out the antennas that had the highest system temperature.

In this work we focus on the observations of the DCO^+ 3–2 and N_2D^+ 3–2 lines from Cycle 0 obsevations, in addition to DCO^+ 5–4, N_2H^+ 5–4 and H_2D^+ $1_{1,0}$–$1_{1,1}$ observations from Cycle 2. Line transitions and frequencies together with peak fluxes and line widths are listed in Table 1.

Additionally, single-dish APEX observations in the ON/OFF mode were carried out on 22 and 24 October 2016 using the heterodyne instrument SheFI with bands APEX-1 (213 – 275 GHz) and APEX-2 (267 – 378 GHz), targeting DCO^+ 3–2 and 5–4, as well as C_2H 4–3. These observations were taken to compare the location of C_2H in both VLA and IRAS, as well as to have a separate verification and comparison of the physical parameters derived from ALMA observations and single-dish. Several transitions of NO and HCN were detected, both of which can form in gas and surface reactions, whereas N_2H^+ and N_2D^+ only form in the gas. NO and HCN are not further analyzed in this work. The pointing was centered on VLA-A (α_{J2000} = 16:26:26.390; $\delta_{J2000} = -24$:24:30.688). The typical RMS noise was 100 mK for APEX-1 and between 50 – 80 mK for APEX-2 in 0.1 km s^{-1} channels. Peak temperatures (T_{mb}) and line widths for Gaussian fits to the single dish lines are listed in Table 1. The typical calibration uncertainties are about 10% for the APEX SheFI instruments in the 230 and 345 GHz bands. The main beam efficiencies used are $\eta_{\mathrm{mb}} = 0.75$ at 230 GHz, and $\eta_{\mathrm{mb}} = 0.73$ at 345 GHz.

Table 3: DCO^+ best approximation model parameters.

Parameter	IRAS 16293-2422	VLA 1623-2417
$T_{\rm peak}$ (K)	17–19	11–16
Drop boundaries:		
$T_{\rm sub}$ (K)	35	35
$n_{\rm de}$ ($\rm cm^{-3}$)	$\leq 10^6$	3×10^6
CO abundance:		
Inner $X_{\rm in}$	10^{-5}	10^{-5}
Drop $X_{\rm D}$	10^{-6}	10^{-7}
Outer X_0	10^{-4}	10^{-4}

4.3 Results

4.3.1 IRAS 16293-2422

The molecules c$-C_3H_2$, C_2H and DCO^+ from the PILS spectral survey (Jørgensen et al. 2016) are considered here, together with DCO^+ and N_2D^+ from the SMA spectral survey (Jørgensen et al. 2011) . The peak intensities and widths of each line are listed in Table 1. Intensity integrated maps of each line overlaid on H_2CO are shown in Fig. 2. H_2CO $5_{1,5}$–$4_{1,4}$ from the PILS survey (van der Wiel et al. in prep.) is used as a reference for the more extended envelope and one of the outflow directions. The nominal velocities at which most species emit at source A and B are $V_{\rm LSR}$ =3.2 and 2.7 km $\rm s^{-1}$. Velocity resolved maps can be found in Appendix 4.A. c$-C_3H_2$ and C_2H spectra at selected positions are presented in Fig. 4 and 5.

DCO^+ is detected in the 5–4 (PILS) and 3–2 (SMA) transitions, with a half-crescent shape centered around source A (Fig. 2 and 3). The peak is red-shifted and located $\sim2''$ south of source A in both transitions. Weak absorption is detected towards source B in the PILS observations. The DCO^+ emission south of source A is weak, peaking at 3 σ in the 5–4 transition and at 5σ in the 3–2 transition. It is slightly extended to the south along the outflow, but not as far as c$-C_3H_2$. In agreement with previous observations of DCO^+ and c$-C_3H_2$ for other objects (Spezzano et al. 2016b,a), these two molecules are spatially anti-correlated.

Five narrow (FWHM $\approx$ 1 km $\rm s^{-1}$) lines of c$-C_3H_2$ with $E_{\rm UP}$ ranging from 48 to 96 K were detected. The emission peaks to the south of A, seen clearly in the top row of Fig. 2. The lines are also seen near source B, at one ALMA beam offset from the source. The southern emission extends from the circumstellar region of source A, and peaks at $\leq5\sigma$ about $\sim4''$ away from the source position. Toward source A itself, the spectrum is too confused to identify the separate molecular lines. Thus the region is masked out in the maps within $2''$ from the source position. Comparing c$-C_3H_2$ with H_2CO (Fig. 2) suggests that it could arise from one side of the southern outflow cavity wall (van der Wiel et al. in prep.). Asymmetrical heating by source A of the outflow cavity could cause only one side to present c$-C_3H_2$ emission. The emission around source B may either be from the circumstellar region or the outflow cavity, but due to the orientation it is difficult to say.

C_2H is clearly detected in both spin doubling transitions with each transition showing a characteristic double hyperfine structure pattern. The emission within $2''$ of source A is masked out due to contamination from other molecular species. C_2H

emission is located in a filament-like structure extending from north to south, passing through source B (Fig. 2). A second, weaker structure formed by a string of clumps extends from north-east to south-west, apparently passing through source A. C_2H is diffuse and weak, peaking at $\lesssim 5\sigma$ on all off-source positions on the map (Fig. 4). The emission around source B is brighter, peaking at 10σ in the intensity integrated map. From the channel map, the emission appears to have a subtle velocity gradient from north to south at source B. However, the C_2H emission does not match the structure and extent of c$-C_3H_2$ (or H_2CO) in either transition (Fig. 4 and 5). It should be noted that neither C_2H or c$-C_3H_2$ coincide with the dust ridge seen in the continuum emission (Fig. 2; see also Jacobsen et al. submitted).

N_2D^+ 3–2 is mostly resolved out in the PILS survey, but it is detected south-east of DCO^+ with the SMA (Fig. 3), located $7''$ away from the continuum position of source A with a S/N = 7 (Jørgensen et al. 2011). Similar to DCO^+, there is no N_2D^+ emission towards B. No transition of N_2D^+ was covered in the Band 7 observations.

4.3.2 VLA 1623-2417

Two transitions of DCO^+ and one transition each of c$-C_3H_2$, N_2H^+ and N_2D^+ were observed with ALMA in Bands 6 and 7, with added ACA observations for Band 6. Additional APEX observations detected two transitions of DCO^+ and C_2H. Intensities and line widths are listed in Table 1. Fig. 6 shows the intensity integrated maps for the ALMA observations. In Appendix 4.A, velocity resolved maps of the ALMA observations can be found. All of these molecules trace material associated with VLA-A, but not the other two components of the system, VLA-B and W.

The DCO^+ 3–2 ALMA 12m array and ACA observations have been analysed in detail in Murillo et al. (2015, see chapter 3). The 3–2 ACA map shows a smooth distribution peaking south-west of the source, with the blue-shifted emission extending north-east, but no clear red-shifted counterpart south-west. Here we present additional ALMA band 7 12m array observations of DCO^+ 5–4. In both transitions of DCO^+ the red-shifted emission, located to the south of VLA-A, is clearly seen and is stronger than the blue-shifted emission located to the north. The DCO^+ 5–4 emission is three times stronger than the 3–2 emission with the 12m array, which makes the blue-shifted emission clearly visible. For both transitions the velocity gradients are consistent. The DCO^+ 3–2 emission borders the disk structure observed to be driven by VLA-A and is relatively compact. Even more interesting, however, is that DCO^+ in the 5–4 transition extends closer to the position of VLA-A than in the 3–2 transition (Fig. 6).

DCO^+ forms at temperatures below 20 K, where CO freezes out. The position of the DCO^+ 3–2 peak along the disk plane was found to be the product of disk-shadowing, which causes a temperature drop at the edge of the disk, whereas along the outflow direction no such effect was observed (Murillo et al. 2015, see chapter 3). The APEX observations of DCO^+ in both transitions show a single peak at the systemic velocity (3.7–4 km s^{-1}) and a peak intensity of 3.6 K for the 3–2 transition, the same as obtained from JCMT observations by Jørgensen et al. (2004). The beamsize for the APEX-1 and 2 bands covers approximately the full extent of the DCO^+ emission seen in the ACA map. For the DCO^+ 3–2 transition, the ALMA observations recover about 28% of the flux detected in the APEX observations (117.1 Jy km s^{-1} with 24 Jy/K), while 20% was recovered with the DCO^+ 5–4 ALMA observations (APEX: 53.7 Jy km s^{-1} with 24 Jy/K).

One low-lying transition of c$-C_3H_2$ is detected with the ACA but not the 12m array. The c$-C_3H_2$ emission is oriented perpendicular to the disk and seems to trace the cavity of the outflow driven by VLA-A out to 3″ from the source position. There is no detection of c$-C_3H_2$ emission in the disk traced by $C^{18}O$ or at the disk-envelope interface, down to the noise level. The material along the outflow cavity exhibits signatures of rotation, most notable in the south-east lobe, with a velocity range and gradient direction similar to that of DCO^+ and $C^{18}O$ (Murillo et al. 2013, see chapter 2).

C_2H is detected with APEX, with the hyperfine components of each transition being clearly distinguished. Both transitions are located at the systemic velocity of VLA-A (3.7–4.0 km s^{-1}) and show no broadening, indicating that the emission is most likely related to the envelope material of VLA-A.

N_2H^+ and N_2D^+ are not detected in our ALMA observations. Possible reasons could be either due to the emission being very extended and thus resolved out in the interferometric observations, or the abundance of these molecules being too low to be detected. This is a surprising contrast to several other young embedded Class 0 sources which do show N_2H^+ and N_2D^+ (Jørgensen et al. 2004; Tobin et al. 2013a). The non-detections of N_2H^+ and N_2D^+ are further analysed in Sect. 4.4.4. H_2D^+ is also not detected in our Cycle 2 band 7 observations, this is consistent with the JCMT observations reported by Friesen et al. (2014). H_2D^+ is not further treated in this work.

4.4 Analysis

4.4.1 DCO^+

DCO^+ appears to peak offset from the protostellar positions bordering the disk-like structures in both sources (Fig. 2 and 6). Here we analyze the peak position first through chemical modelling of the observed emission, and then using the line ratios to constrain the physical structure (temperature, density) and the associated chemistry.

DCO^+ distribution

In Murillo et al. (2015, see chapter 3) the distribution of DCO^+ around VLA was found to be altered by the presence of a rotationally supported disk, causing the emission to move inwards along the disk plane but not along other directions. In this section, the DCO^+ emission around IRAS is modelled, aiming to find whether the distribution of DCO^+ in IRAS is product of the same phenomenon as observed in VLA.

The DCO^+ chemistry is particularly sensitive to temperature. To model the observed emission for IRAS and VLA, a simple steady-state, analytic chemical network that accounts for the basic reactions leading to the production and destruction of DCO^+ is used.

Since CO and H_2D^+ are the precursors of DCO^+, the production of H_2D^+ will be the rate-determining reaction in the chemical network, since it will dictate the production of DCO^+. The H_2D^+ production and destruction reaction is given by

$$H_3{}^+ + HD \underset{\Delta E}{\rightleftharpoons} H_2D^+ + H_2 \tag{4.1}$$

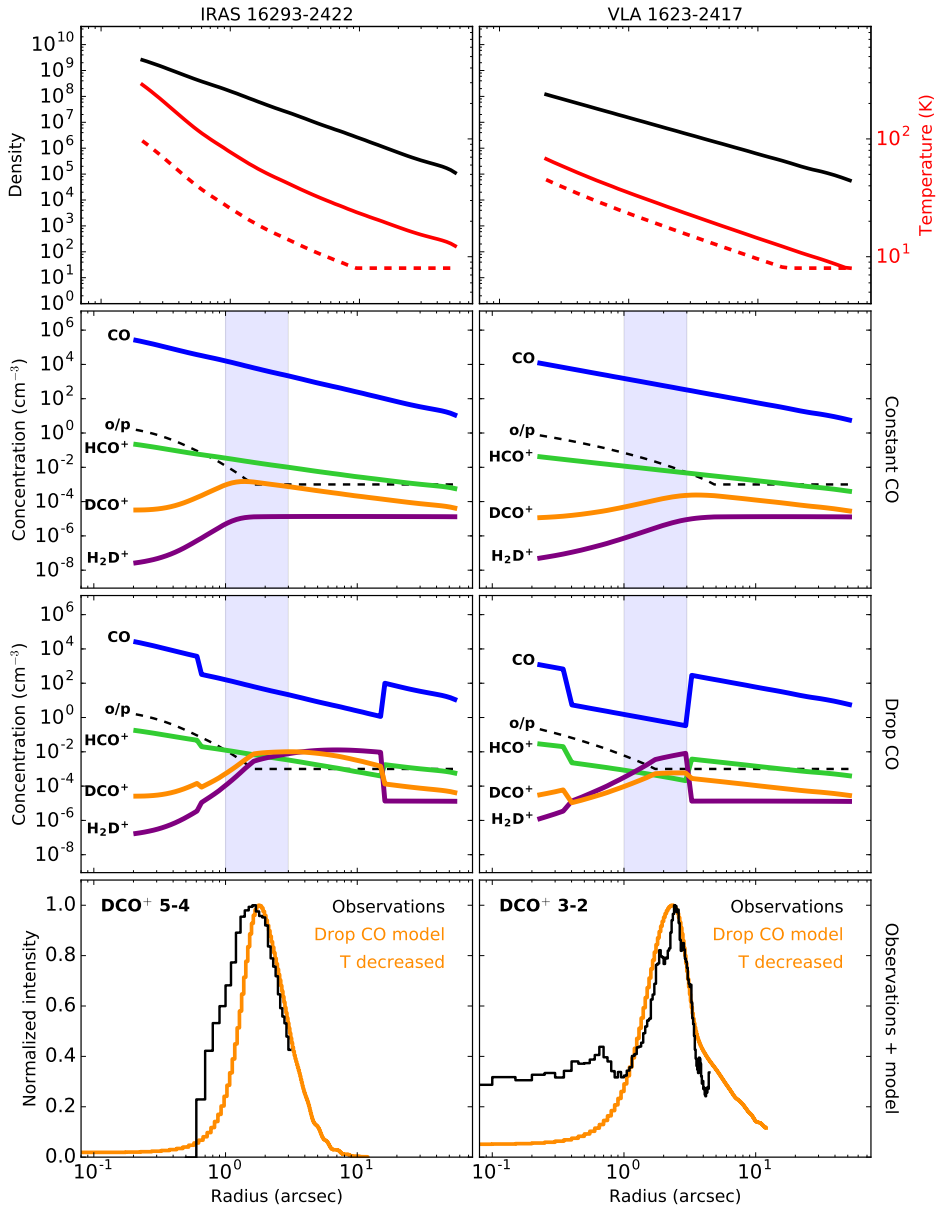

Figure 8: Results from modelling the observed DCO^+ peak with our simple analytic chemical model. The left column shows results for IRAS 16293-2422, while the right column shows those for VLA 1623-2417. The top row shows the input density (black) and temperature (red) as functions of radius for each system. The dashed red line shows the original temperature profile used for the constant CO model (second row panels). This model does not show a DCO^+ peak at the right position. The solid red line is the profile decreased by factors of 3 and 1.5 for IRAS 16293-2422 and VLA 1623-2417, respectively, and used for the drop CO model (third row panels). The lower limit on the temperature is set at 8K. In the second and third row, the shaded range is the location of the observed DCO^+ peak. The bottom row shows the observed radial profiles of DCO^+ overlaid with the Drop CO model.

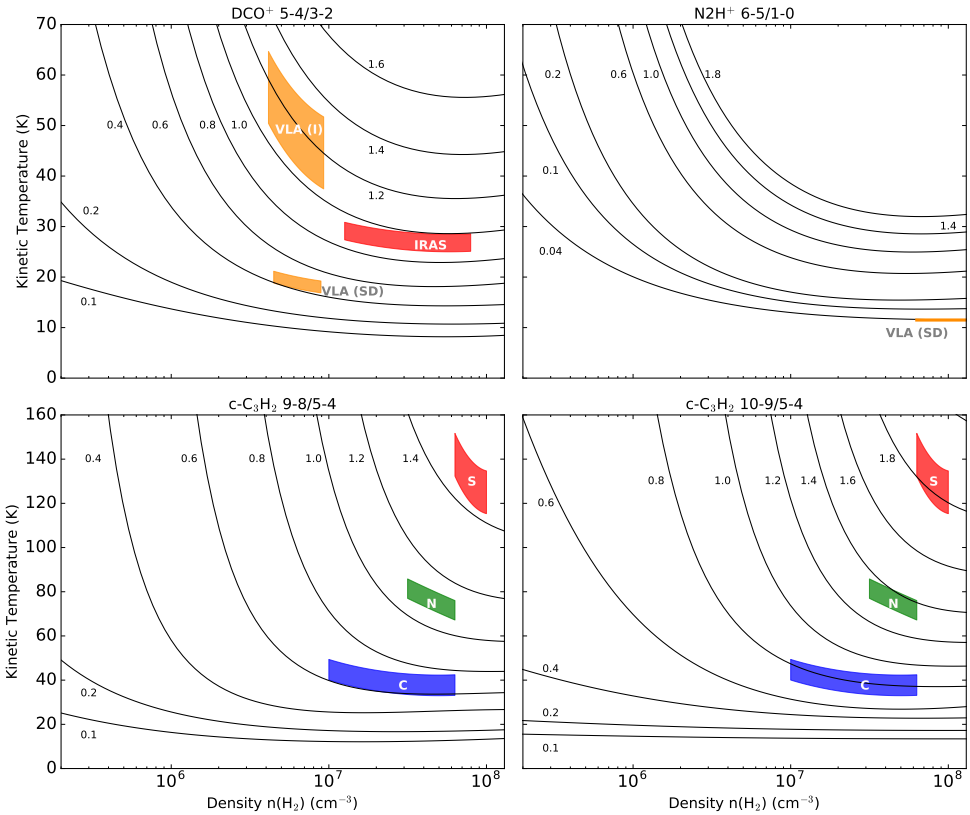

Figure 9: Calculated line ratios for DCO^+ 5–4/3–2, N_2H^+ 6–5/1–0 and c$-C_3H_2$ 10–9/5–4 and 9–8/5–4. Black lines show the modelled ratios assuming column densities of 2.5×10^{12} and 1.3×10^{13} cm^{-2} for DCO^+ and N_2H^+, respectively, and 2.5×10^{13} for both c$-C_3H_2$ ratios. Color areas indicate the observed line ratios drawn over the range of densities and temperatures that characterize the observed emission, for IRAS 16293-2422 with ALMA (red, blue and green) and VLA 1623-2417 (orange) with single-dish (SD) and interferometric (I) observations.

Table 4: DCO^+ intensities and line ratios, with inferred temperature and density.

Source	IRAS 16293-2422		VLA 1623-2417 - ALMA		VLA 1623-2417 - APEX	
Transition	5–4	3–2	5–4	3–2	5–4	3–2
Line width (km s^{-1})	1.0	1.0	0.6	0.6	0.7	0.7
Beam (arcsec)	0.5×0.5	4.11×2.45	0.87×0.65	0.85×0.54	17.3	28.9
Peak (Jy $beam^{-1}$)	5.3±0.4	1.8±0.2	0.29±0.02	0.087±0.008	...	...
Peak (K)	4.0±0.3	4.7±0.5	4.8±0.3	4.9±0.5	2.2±0.1	4.8±0.1
Line ratio	0.9±0.1		1.0±0.1		0.46±0.03	
Column density (cm^{-2})	3×10^{12}		2×10^{12}		2×10^{12}	
H_2 density (cm^{-3})	$1–8\times10^{7}$		$2–6\times10^{6}$		$4–9\times10^{6}$	
T_{kin} (K)	26–29		30–55		18–20	
τ	<1		<1		<1	

Table 5: c$-C_3H_2$ inferred parameters and abundance ratio for c$-C_3H_2/C_2H$

Position	Coordinates		9–8/5–4	10–9/5–4	n_{H_2}	T_{kin}	$N_{c-C_3H_2}$ [a, b]	N_{C_2H} [a]	c$-C_3H_2/C_2H$
	RA	Dec			cm^{-3}	K	cm^{-2}	cm^{-2}	
IRAS 16293-2422									
South	16:32:22.88	–24:28:39.78	1.7±0.08	1.4±0.07	5–10×10^7	120–155	9.3×10^{13}	3×10^{13}	≥3.1
Center	16:32:22.69	–24:28:35.16	0.7±0.3	0.7±0.3	1–6×10^7	37–44	1.3×10^{13}	2×10^{14}	≤0.07
North	16:32:22.55	–24:28:30.28	1.6±0.6	1.3±0.5	3–6×10^7	71–81	1.1×10^{13}	2×10^{14}	≤0.05
VLA 1623-2417					c$-C_3H_2$	$3_{3,0}$–$2_{2,1}$			
c$-C_3H_2$ [c]	16:26:26.39	–24:24:30.69	...	...	5–10×10^7	120–155	2.7–5.3×10^{13}	1–1.5×10^{13}	2.7–3.5

Notes. [a] For IRAS 16293-2422, column densities are for a beam of 0.5″. For VLA 1623-2417, column densities are for a beam of 1.6″ ×0.88″ for c$-C_3H_2$ and 17.3″ for C_2H. [b] An o/p = 3 was used to calculate the total column density of c$-C_3H_2$. [c] c$-C_3H_2$ parameters from the south position of IRAS 16293-2422 .

where the activation energy $\Delta E \sim 220$ K in the back reaction is due to the difference in zero-point energy. A crucial factor for deuterium chemistry is the ortho-to-para ratio of H_2 (Flower et al. 2006; Pagani et al. 2009b). This is included in the back reaction of the chemical network (Eq. 4.1), since it is here where the distinction has the most significant effect (Murillo et al. 2015, see chapter 3). The reactions and parameters for o$-H_2$ and p-H_2 were adapted from Walmsley et al. (2004). The ortho-to-para ratio is set to have a lower limit of 10^{-3} at low temperatures, as constrained from observations and models (Flower et al. 2006). The rate coefficient for two-body reaction is expressed as

$$k = \alpha \left(\frac{T}{300}\right)^{\beta} \exp\left(-\frac{\gamma}{T}\right) \text{ cm}^3 \text{ s}^{-1} \tag{4.2}$$

where T is the temperature of the gas. For cosmic ray ionization, important in the generation of $H_3{}^+$, the rate coefficient is given by

$$k = \zeta \text{ s}^{-1} \tag{4.3}$$

where $\zeta = 1.26 \times 10^{-17}$ is the cosmic-ray ionization rate of H_2. The reactions and rate coefficients used in this work are the same as those listed in Murillo et al. (2015, see chapter 3).

Since CO is a parent molecule of DCO^+, its abundance will impact the production of DCO^+. The profile of the CO abundance is taken to be either constant or with a drop used to simulate freeze-out. The drop is set by the CO sublimation temperature $T_{\rm sub}$ and desorption density $n_{\rm de}$. These limits dictate the boundary where CO is in the gas phase ($T > T_{\rm sub}$) or freezes onto the dust grains ($T < T_{\rm sub}$); and when the freeze-out time-scales for CO are too long ($n < n_{\rm de}$) compared to the lifetime of the core (Jørgensen et al. 2005c). The results of the chemical modelling are passed through RATRAN (Hogerheijde & van der Tak 2000), and then synthetic data cubes are generated in order to directly compare with the observations. The network and further details of the model and post-processing are given in Murillo et al. (2015, see chapter 3).

The model requires a density and temperature profile of the source as a function of radius. For IRAS, the power-law density and temperature profile from Crimier et al. (2010) is adopted. Two assumptions are made, namely that the density and temperature profile is centred on IRAS-A and that it is the main contributor to the luminosity of the core, consistent with the recent analysis of Jacobsen et al. (submitted). Thus, our assumptions should not introduce major issues in our modelling. While there have been several physical profiles derived for IRAS (e.g., Schöier et al. 2002), only one is adopted here since we alter the density and temperature profiles by an arbitrary factor, exploring the effects of these parameters on the production of DCO^+. For VLA, we adopt the power-law density and temperature profile from Jørgensen et al. (2002). Here again we assume the density and temperature profile is centred and dominated by VLA-A. Given that VLA-B does not contribute much to the line emission nor the continuum, and that VLA-W is $10''$ away, this should not produce issues in the resulting model. The temperature and density profile for VLA is also altered by an arbitrary factor to study the effect on DCO^+ production. The variations in the temperature and density profiles used in this work are listed in Table 2 for both systems.

For the DCO^+ models, we explore the parameter ranges of T_{sub} = 20–40 K, n_{de} = 10^5–10^8 cm^{-3} and X[CO] = 10^{-7} – 10^{-4}. The parameters for the best by-eye approximation to the observed DCO^+ peak position are listed in Table 3 for both systems. The best approximated model of the DCO^+ 3–2 emission around VLA (Murillo et al. 2015, see chapter 3) are reproduced here and compared with the results of DCO^+ toward IRAS.

For both systems we find that the constant CO abundance profile does not produce a DCO^+ peak where observed (too far outward), and the peak position does not shift with a change in the abundance. The drop CO abundance profile produces a peak within the drop boundaries, T_{sub} and n_{de}. Altering these parameters changes the shape but not the position of the DCO^+ peak.

Since the chemical conditions do not alter the peak position, the physical structure is examined. The original source density and temperature profiles for both sources also do not reproduce the position of the DCO^+ peak. Increasing or decreasing the density by one order of magnitude, causes the DCO^+ peak to either shift outwards or remain at a position similar to the unchanged density profile. Interestingly, only reducing the temperature profile by an arbitrary factor together with the drop CO abundance profile, causes the DCO^+ peak to shift inwards for both systems (Fig. 8). This is consistent with the results found for VLA's DCO^+ 3–2 in Murillo et al. (2015, see chapter 3), which explores the physical and chemical parameter space in more detail. Thus the observed DCO^+ peak position is produced by a drop in the temperature along the plane perpendicular to the outflow(s). This drop in temperature can be caused by a structure, such as a disk, which shadows the outer regions, allowing the peak emission of molecules whose abundance is enhanced in cold gas to move inwards.

It should be noted, however, that our simple chemical model cannot fully explain the inner part of the DCO^+ 5–4 emission observed centered on VLA-A. DCO^+ 5–4 emission at small radii could be located in the disk where both cold and warm chemical processes can contribute to its formation (Favre et al. 2015; Huang et al. 2017; Salinas et al. 2017).

Thus, the distribution of DCO^+ around both VLA and IRAS is product of the presence of a disk(-like) structure, which causes a drop in temperature on the envelope gas at the edge of the disk(-like structure), i.e. the disk-envelope interface. The presence of the disk(-like) structure generates an asymmetric temperature profile in the protostellar system.

Line ratios and implied physical conditions

Line ratios can provide an independent measure of the temperature of the region being traced by a molecule. The ratio of DCO^+ 5–4/3–2 will provide an independent test of the results obtained with the chemical model of DCO^+ described in the previous section.

Using RADEX (van der Tak et al. 2007), we performed non-LTE excitation and radiative transfer calculations to constrain the temperature and density of the regions being traced by comparing the ratios of observed molecular lines with those calculated by the non-LTE excitation. We limit the range of H_2 densities based on the source profile used for chemical modelling (Table 2 and Fig. 8) and the radial position of the emission being modelled. We assume the optically thin regime for all cases, which is valid for all low abundance species considered here. In this regime, the adopted column density does not affect the line flux ratios, only the absolute flux values. The

molecular data files are obtained from the Leiden Atomic and Molecular Database (LAMDA; Schöier et al. 2005b). In order to compare the observed peak intensities with the results from RADEX, the observed peaks are converted from Jy beam^{-1} to K using the relation $T_{\rm mb} = 1.36\ \lambda^2/\theta^2\ S_{\rm observed}$ where λ is the wavelength in centimetres of the molecular transition, θ is the beam of the observations and $S_{\rm observed}$ is the observed flux density in mJy beam^{-1}.

Here, we derive the physical parameters from the DCO^+ 5–4/3–2 ratio for both sources. Figure 9 shows the variation of the DCO^+ 5–4/3–2 ratio with H_2 density and temperature. For both IRAS and VLA, the red-shifted peak emission is considered, since it is the most prominent. The results for IRAS and VLA are compared in Table 4.

For IRAS, a ratio DCO^+ 5–4/3–2 = 0.9 ± 0.09 is obtained from the PILS band 7 observations and the SMA 230 GHz observations (Jørgensen et al. 2011). We adopt a line width of 1.0 km s^{-1} and a column density of 3×10^{12} cm^{-2}, a value that also reproduces the observed line intensities. For densities below 10^6 cm^{-3}, the critical density of the 5–4 transition, the line ratio is primarily sensitive to density; at higher densities, the ratio becomes a good temperature probe. According to the density structure presented in Fig. 8 (top panel), the density at the peak DCO^+ emission position is higher than the critical density, so a kinetic temperature between 20 and 30 K can be inferred for IRAS. This temperature is consistent with the chemical modelling of the DCO^+ peak position.

For VLA, the ALMA 12m array observations provide DCO^+ 5–4/3–2 = 1.0 ± 0.1. The beam-size of DCO^+ 5–4 ($0.87'' \times 0.65''$) is similar to that of the 3–2 transition ($0.87'' \times 0.54''$) and thus no beam dilution factor was added to the calculation. This line flux ratio implies a kinetic temperature between 30 and 55 K, adopting a column density of 2×10^{12} and a line width of 0.7 km s^{-1} to reproduce the observed peak intensities. This is higher than expected from the chemical modelling of DCO^+. The APEX observations are used to double check if this is the kinetic temperature of the bulk of the DCO^+ emission at the disk-envelope interface. The APEX DCO^+ data give a much lower line ratio, 5–4/3–2 = 0.46 ± 0.03. This line flux ratio is well reproduced by a kinetic temperature of 17 to 19 K, in agreement with the chemical model. It is likely that the ALMA 12m array observations are picking up both warm and cold DCO^+ emission in the 5–4 transition, but only cold DCO^+ in the 3–2 transition. On the other hand, the APEX observations are recovering DCO^+ emission from the cold regions at the edge of the disk and the envelope, but the beam size dilutes the emission from the inner regions. This then causes the discrepancy of derived kinetic temperatures that we obtain from interferometric versus single-dish data. The temperature from the interferometric data is driven up due to more emission being detected in the higher transition.

4.4.2 c$-C_3H_2$

To study the physical conditions of the region traced by c$-C_3H_2$, line ratios of the detected transitions, rather than chemical models, are used. Five transitions of c$-C_3H_2$ are detected towards IRAS. Temperature and density are derived from the c$-C_3H_2$ 9–8/5–4 and 10–9/5–4 ratios (See Sect. 4.4.1). Figure 9 shows the line flux ratios as functions of H_2 density and kinetic temperature. The ortho-c$-C_3H_2$ molecular file is used for the RADEX calculations since the 5–4 transition (349.264 GHz) presented here is the ortho form (para-c$-C_3H_2$ 5–4 is at 338.204 GHz). To convert to the total

(ortho + para) c−C_3H_2 column density, an o/p ratio of 3 was used. Three regions covering the south c−C_3H_2 peak and the C_2H peaks near the center and north of the map are selected to derive the temperature and c−C_3H_2/C_2H column density ratios (Fig. 4). Table 5 lists the positions. The IRAS-A and B positions are not modelled due to contamination from other molecular species.

Both c−C_3H_2 9–8/5–4 and 10–9/5–4 ratios are simultaneously fit for each position. Table 5 lists the ratios along with the adopted densities and derived kinetic temperature. The peak intensities for each transition at the three positions are listed in Table 6 We find that the temperature for the south c−C_3H_2 peak, corresponding to the outflow cavity of IRAS-A, is between 120–155 K, 2 to 4 times higher than for the positions where C_2H peaks. The central position shows the lowest temperature with 41–44 K. Comparing the temperatures obtained from c−C_3H_2 and DCO^+ line ratios, it is clear that c−C_3H_2 arises from a much warmer region than DCO^+. This is linked to the spatial anti-correlation found for these two molecules, both in our observations and other work (see Sect. 4.5).

Only one transition of c−C_3H_2 is available for VLA, with an upper level energy (19.5 K) lower than those observed toward IRAS ($\geq$ 49 K). Thus to obtain an idea of the column densities in the region traced by c−C_3H_2 towards VLA, we adopt the temperature and density from the c−C_3H_2 line ratios towards IRAS at the south peak. The c−C_3H_2 south peak of IRAS is chosen due to the fact that it traces the outflow cavity, as it does for VLA. Using the parameters of c−C_3H_2 from IRAS, the derived column density is a few times 10^{13} cm^{-2}, lower by about a factor of 2 or 3 than that found for the south peak of IRAS and similar to the column density found for the central position of the IRAS map.

4.4.3 C_2H

The same transitions of C_2H are observed towards both sources, with ALMA for IRAS and with APEX for VLA. The peak intensities are listed in Table 6. Since C_2H ratios are not sensitive to temperature or density given the similar upper eneriges E_{up} (Table 1), the method adopted for DCO^+ and c−C_3H_2 cannot be used here. Instead, the C_2H column density is derived by assuming the kinetic temperature and number density obtained from c−C_3H_2 line ratios. The results are listed in Table 5.

The south position in IRAS presents a column density of $\leq 3\times10^{13}$ cm^{-2}, about an order of magnitude lower compared to the centre and north positions which have a column density of 2×10^{14} cm^{-2}. Table 5 lists the c−C_3H_2/C_2H column density ratio for each position. It must be noted that the ratio at the south position is a lower limit, whereas for the central and north position, it is an upper limit. The differences in ratios between positions reflect the anti-correlation of the two molecules in the IRAS system. Most certainly, the anti-correlation is not due to critical densities, since the derived number densities of c−C_3H_2 (10^7 to 10^8 cm^{-3}) at all points are above the critical densities of both C_2H (8×10^4 to 6×10^5 cm^{-3}) and c−C_3H_2 (2–5×10^5 cm^{-3}).

For VLA, C_2H column densities are found to be a few times 10^{13} cm^{-2}, lower than the peaks of C_2H detected towards IRAS. The results are listed in Table 5. The c−C_3H_2/C_2H ratio of column density provides values similar to the south position towards IRAS.

4.4.4 N_2H^+ and N_2D^+

For VLA, the ALMA 12m array observations of N_2D^+ and N_2H^+ did not detect any emission. Since these molecules are readily detected in other sources (e.g., Tobin et al. 2013a), the cause of this non-detection is examined. Two cases are explored, extended and compact emission concentrated in a 1″ region. The details of the analysis are given in Appendix 4.B.

For the case of extended emission, the predicted N_2H^+ 4–3 peak intensity is the same as the noise level of our observations, while for the case of the emission concentrated in 1″ region, the S/N would be about 26. In a similar manner, the predicted N_2D^+ 3–2 peak intensity is expected to have a marginal detection in our observations for the extended emission case, and a $S/N = 40$ for the compact emission case. Thus, we should have detected both molecules in our observations if they arose from a compact structure.

4.5 Discussion

4.5.1 Comparison of IRAS 16293-2422 and VLA 1623-2417

The chemical structure of both systems is compared in this section. A cartoon of their structure is shown in Fig. 1.

The DCO^+ peak position in both sources is well described by a drop in the temperature profile. This drop can be explained by the presence of a disk which shadows the envelope, causing the DCO^+ emission to move inward, closer to the source along the disk plane. For VLA, the ALMA DCO^+ 5–4 observations are picking up emission coming from both the cold envelope at the edge of the disk (disk-envelope interface) and the warmer parts of the disk.

c$-C_3H_2$ traces the outflow cavity of IRAS-A and VLA-A. For VLA-A, c$-C_3H_2$ traces the full outflow cavity (extending out to 3″), whereas for IRAS-A only one side of the south outflow cavity wall is observed. It is possible that the c$-C_3H_2$ emission is product of UV radiation from the central source, and the warmer temperatures found in the outflow cavity. UV radiation liberates atomic carbon which leads to gas-phase formation of small hydrocarbons. Chemical models of the outflow cavity walls show that c$-C_3H_2$ is initially concentrated around the outflow wall, and progressively moves to the disk plane as the cavity widens with age, irradiating more envelope material (Drozdovskaya et al. 2015). Higher temperatures could accelerate certain chemical processes in the protostellar envelope, while movement of material through outflows, rotation and infall could bring dust with c$-C_3H_2$ precursors (e.g., CH_4, C_2H_2) closer to areas where they can be sublimated and thus enhance the c$-C_3H_2$ gas. Hence, the differences in the spatial distributions of c$-C_3H_2$ in IRAS-A ($L_{\rm bol} > 18$ L$_\odot$, Jacobsen et al. submitted) and VLA-A ($L_{\rm bol} \sim 1 L_\odot$) could be the product of age, luminosity, or core dynamics. In any case, the presence of c$-C_3H_2$ emission is due to the temperature of the region where it is observed.

C_2H does not present similar distributions in IRAS and VLA. Toward VLA, the single-dish C_2H emission peaks on VLA-A, and is most likely spatially correlated with c$-C_3H_2$. C_2H could arise from the envelope or outflow, given that it shows similar broadening with DCO^+ (Lindberg et al. 2017), but also with c$-C_3H_2$. For IRAS, the observed C_2H is found in the region one beam away from IRAS-B, but does not show

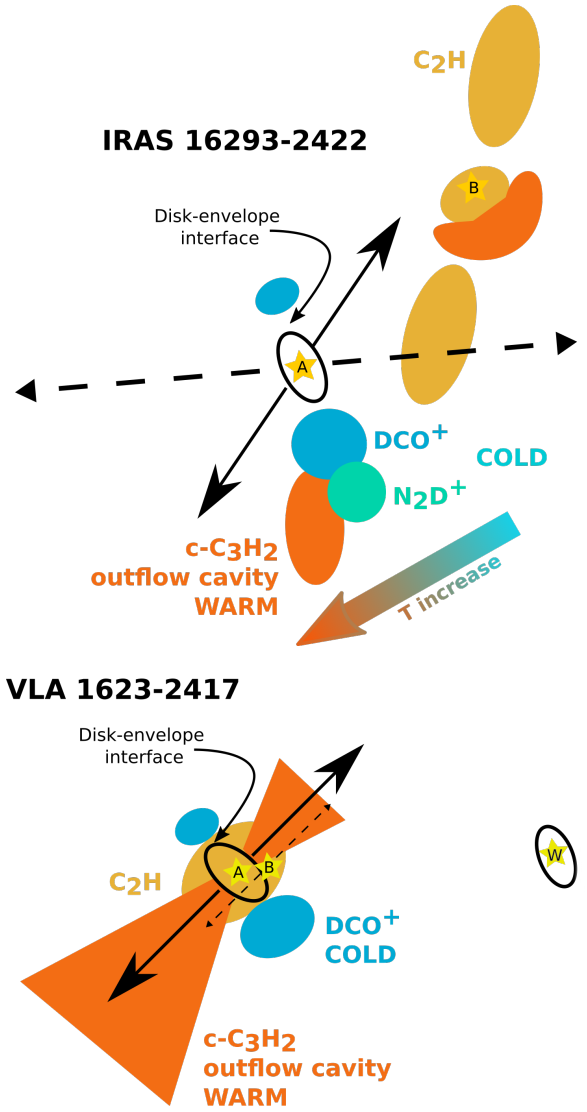

Figure 10: Cartoon showing the distribution of the molecules studied in this work towards both sources. The solid and dashed lines show outflow directions. Ellipses indicate disk structures.

relation with the position or outflow of IRAS-A, nor with the dust ridge connecting both sources. Beyond IRAS-B, C_2H and c$-C_3H_2$ are not spatially correlated (Fig. 4 and 5). This anti-correlation is unexpected from chemical models (e.g. Gerin et al. 2011; Drozdovskaya et al. 2015; Guzmán et al. 2015) or observations (see Sect. 4.5.2). The c$-C_3H_2/C_2H$ ratio is expected to be lowered with age, that is as the protostar evolves (O. Sipilä, private communication). If the different distributions of c$-C_3H_2$ and C_2H are product of age, it would suggest that IRAS is somewhat older than VLA; however, lowering the ratio with age does not explain the anti-correlation observed in IRAS.

A possible explanation may be top-down chemistry producing small hydrocarbons through UV destruction of large aromatic molecules as inferred for lower density PDRs (Guzmán et al. 2015), producing different amounts of the two molecules. Another possibility for the anti-correlation might be explained by the destruction of C_2H in reactions with sulfur, nitrogen, oxygen or carbon chains (Sakai & Yamamoto 2013). The full Band 7 spectrum is examined at the c$-C_3H_2$ peak position (Fig. 13– 15) in order to examine whether products of C_2H reactions are present. C_2S, product of C_2H reacting with sulfur (Drozdovskaya et al. in prep.), is not detected. In fact, little else is observed in the dense gas south of IRAS-A. Apart from c$-C_3H_2$, only H_2CS (Drozdovskaya et al. in prep.) and a few common species like HCO^+, H_2CO and CH_2OH are detected, which is unexpected given that outflow cavity would be irradiated and encourage chemical complexity (Drozdovskaya et al. 2015). Reactions of C_2H with carbon chains C_n would cause production of C_{n+2} and hydrogen, rendering these products undetectable due to lack of dipole moments. Overall, the strong anti-correlation of these molecules remains a chemical puzzle.

N_2D^+ is detected 7″ south of IRAS-A with the SMA (Fig. 3), bordering the DCO^+ emission (Jørgensen et al. 2011). In contrast, N_2D^+ and N_2H^+ are not detected with ALMA observations towards VLA. Single-dish observations show an offset between the position of VLA and the peak of N_2H^+ and N_2D^+ (Di Francesco et al. 2004; Liseau et al. 2015; Punanova et al. 2016; Favre et al. 2017). Since neither molecule is detected in our observations with ALMA (Sect. 4.4.4), it would suggest that N_2H^+ and N_2D^+ lines trace emission outside the VLA envelope (Liseau et al. 2015).

The presence of N_2D^+ in IRAS, but not in VLA, could be product of temperature differences. N_2 can be frozen out onto dust grains at temperatures below 20 K (Bisschop et al. 2006), a scenario also pointed out by Di Francesco et al. (2004). While other nitrogen-bearing molecules such as CN, HCN, HNC and NO can form in the gas and on grain surfaces, N_2H^+ and N_2D^+ only form in the gas phase if N_2 gas is present. This scenario is further supported by the low temperatures found for DCO^+. For VLA-A, DCO^+ has $T_{\rm kin}$ = 17 K, and the chemical modelling suggests dust temperatures between 11 to 16 K for where DCO^+ peaks. This would indicate that further out, the temperature is even lower. In addition, at densities below $\sim 10^4$ cm^{-3}, the dust and gas temperatures decouple, and without any additional external pressure, the gas temperature drops down to 10 K (Galli et al. 2002; Evans et al. 2001), which could cause N_2H^+ and N_2D^+ to recombine onto the dust grains or the precursor N_2 to freeze-out. In contrast, DCO^+ south of IRAS-A indicates $T_{\rm kin}$ = 30 K for the gas, and dust temperatures between 17 to 19 K from chemical modelling, evidencing that the envelope of IRAS-A is warmer than that of VLA (Jacobsen et al. submitted).

N_2H^+ and N_2D^+ are thought to be tracers of evolutionary stage (Emprechtinger

et al. 2009), as well as of the CO snowline (Jørgensen et al. 2004; Anderl et al. 2016; van't Hoff et al. 2017). These assumptions break down for very cold envelopes like that of VLA. Given that some starless cores do show N_2H^+ and N_2D^+ (Tobin et al. 2013a), including the starless cores north of VLA (Di Francesco et al. 2004), it cannot be said that the cold envelope itself is an indicator of evolutionary stage. It may be possible that the ridge of material north of VLA, which contains the starless cores, is being heated somehow from the side, but VLA is being shielded and thus much colder (Di Francesco et al. 2004; Bergman et al. 2011; Friesen et al. 2014). VLA-A itself is certainly heating up the disk and outflow cavity, evidenced by DCO^+ 5–4 emission on the disk and the presence of c$-C_3H_2$, but on much smaller scales (<100 AU) than in IRAS because of its lower luminosity.

4.5.2 Comparison with starless cores and low-mass protostars

In this section, IRAS and VLA are placed in the big picture of star formation. For this reason, the two systems described in the previous section are compared with observations of starless cores, embedded low-mass protostars and disks found in the literature. In addition, the multiplicity of the systems is also taken into consideration.

The starless core L1544 exhibits c$-C_3H_2$ close to the dense cloud core center and away from cold regions traced by DCO^+ (Spezzano et al. 2016b,a). This points to an anti-correlation between the chemistry traced by DCO^+ and that by c$-C_3H_2$, which is present in both IRAS and VLA. In the system NGC1333 IRAS4, C_2H is observed to peak on-source toward each component, including the starless core IRAS4C, which has the strongest emission (Koumpia et al. 2016, 2017). In the young embedded object IRAS15398, C_2H traces the red- and blue-shifted outflow cavity (Jørgensen et al. 2013). In contrast, L1527 presents both C_2H and c$-C_3H_2$ in the envelope and disk component, with enhancements at the centrifugal barrier (Sakai et al. 2010, 2014b, 2016), but no emission along the outflow cavity. The spatial distribution of C_2H and c$-C_3H_2$ is similar in L1527, with the emission from c$-C_3H_2$ being more compact than that of C_2H. In Oph-IRS67, C_2H and c$-C_3H_2$ exist in the same region, although the spatial extent is not the same (Artur de la Villarmois et al. submitted). In the protoplanetary disk TW Hya, C_2H and c$-C_3H_2$ are found to reside in the disk, bordering the millimeter dust, with both molecules showing an identical spatial distribution (Bergin et al. 2016). The c$-C_3H_2$ and C_2H distribution toward VLA is consistent with that observed in other protostellar systems; however, for IRAS the lack of correlation between the two molecules is still a puzzle, since no other source presents this situation.

In NGC1333 SVS13, N_2H^+ is detected around 2 of the 4 components of the system (Chen et al. 2009). From the system, SVS13B and SVS13C are Class 0 protostars, but the first has N_2H^+ emission while the second does not. Thus, the uneven distribution of material is not related to the evolutionary stage, but instead is most likely related to the varying envelope temperature.

Several of the systems mentioned above are multiple protostars, as are IRAS and VLA. The chemical structure is found to not be homogeneous among the individual components of these systems. Thus multiplicity in the embedded phase does not seem to affect the observed chemical structure, that is external heating from companions appears to have no significant effect. Altogether, the chemical structure of embedded protostellar systems for the molecules studied here seems to not be dependent on the

evolutionary stage, parent cloud or companion sources, but primarily on the central source heating its surrounding gas.

4.5.3 Comparison with diffuse clouds, PDRs and high-mass protostars

Looking to compare what structures are common throughout the interstellar medium, we compare the distributions found in IRAS and VLA with diffuse clouds and PDRs. Furthermore, given that IRAS is much warmer than VLA, it is also compared to high-mass protostars.

Towards the Horsehead nebula PDR, DCO^+ is observed far from the irradiated edge of the region, with no emission at the edge (Guzmán et al. 2015). The spatial anti-correlation between DCO^+ and c$-C_3H_2$ or C_2H suggests a temperature effect, as found for IRAS and VLA, highlighting that DCO^+ is a really good tracer of cold regions.

c$-C_3H_2$ and C_2H show close correlation in spatial distribution towards a number of PDRs, including the Orion Bar (Pety et al. 2007; van der Wiel et al. 2009; Nagy et al. 2015) and the Horsehead Nebula (Cuadrado et al. 2015; Guzmán et al. 2015), with both molecular species sitting at the irradiated, and thus warmer, edge of the region. In addition, a tight correlation between c$-C_3H_2$ and C_2H in diffuse clouds has been found (Lucas & Liszt 2000; Gerin et al. 2011; Liszt et al. 2012). The column density c$-C_3H_2/C_2H$ ratios calculated toward IRAS in the center and north positions (c$-C_3H_2/C_2H$ = 0.05–0.07) reflect the values found for diffuse clouds (c$-C_3H_2/C_2H$ = 0.048; Lucas & Liszt 2000; Liszt et al. 2012) and the envelope of L1527 (c$-C_3H_2/C_2H$ = 0.035 – 0.06; Sakai et al. 2014b).

In high-mass star-forming regions, c$-C_3H_2$ and C_2H are also strongly correlated, with both lines presenting similar spatial distributions (Pilleri et al. 2013; Mookerjea et al. 2012, 2014). Thus, the warmer envelope of IRAS does not provide a solution to the puzzle of why c$-C_3H_2$ and C_2H are anti-correlated in this system. The cause is most likely not related to the physical structure of IRAS, but the chemical processes occurring in the envelope of this system.

4.6 Conclusions

In this work, we present ALMA, SMA and APEX observations of DCO^+, c$-C_3H_2$, C_2H, N_2H^+ and N_2D^+ towards IRAS 16293-2422 and VLA 1623-2417, both multiple protostellar systems in ρ Ophiuchus. The spatial distribution of each molecule is compared for both systems. DCO^+ is studied using a simple analytic chemical network coupled with radiative transfer modelling, detailed in Murillo et al. (2015, see chapter 3), in order to determine the conditions leading to the observed peak position. Non-LTE molecular excitation and radiative transfer modelling of the observed line flux ratios is done to derive physical parameters of the regions being traced by the molecules. Finally, the observations and results of VLA 1623-2417 and IRAS 16293-2422 are compared, both between the two sources and other objects, ranging from low- to high-mass protostars, diffuse clouds and PDRs, in order to understand what structures are common.

From this work, we extract the following key points:

1. Temperature is a controlling factor of the chemical structure of a protostellar system. Disks can alter the temperature of the envelope, while UV heating can encourage the start of chemical processes in the outflow cavity.

2. An asymmetric DCO^+ structure is a good tell-tale sign for the presence of a disk, since a disk shadows the envelope at its edge, lowering the temperature and causing DCO^+ to move inwards only along the disk plane.

3. c$-C_3H_2$ traces the outflow cavity of IRAS 16293-2422 and VLA 1623-2417, but shows no disk component for either source.

4. Despite both VLA 1623-2417 and IRAS 16293-2422 being low-mass Class 0 embedded objects, their structure and chemical richness varies considerably, with VLA 1623-2417 being line poor. Its much lower luminosity, and consequently lower temperatures, coupled with a large cold disk, are likely at the root of this difference.

Although only two sources are studied in this work and some results in the literature, there is evidence pointing to a lack of correlation between multiplicity and the chemical structure of the envelope of these systems, at least in the embedded phase. Nevertheless, multiple systems do provide an interesting way to compare the structure with similar conditions. It would be possible, however, that the heating from companion sources would affect the chemistry as the envelope clears. Further comparison of embedded multiple protostellar systems is needed to confirm these results.

Appendix

4.A Velocity integrated maps

The velocity integrated maps of the molecules presented in this work are shown in Fig. 11. For IRAS 16293-2422 A, the velocity gradient goes from north-east (blue-shifted) to south-west (red-shifted). This gradient is consistent for H_2CO and all the transitions of c$-C_3H_2$. DCO^+ is only observed to have a red-shifted component. This is consistent with the DCO^+ observations with the SMA and ACA. The velocity gradient of IRAS 16293-2422 B is less clear, which is most likely due to it being orientated face-on.

4.B Peak intensities and line ratios

The observed peak intensities of C_2H and c$-C_3H_2$ are listed in this appendix (Table 6). The peak intensities are used in Sect. 4.4.2 and 4.4.3. In addition, the detailed calculation of expected peak fluxes for N_2H^+ and N_2D^+ are also summarized here (Table 7).

Single-dish observations of low-J transitions of CN, HCN and HNC show strong detections relative to other embedded systems (Jørgensen et al. 2004). Our recent APEX observations also detected NO towards VLA. However, single-dish observations of NH_3 (Wootten et al. 1994; Liseau et al. 2003) and N_2H^+ (Liseau et al. 2015; Punanova et al. 2016) indicate that these molecules have very low abundances at the

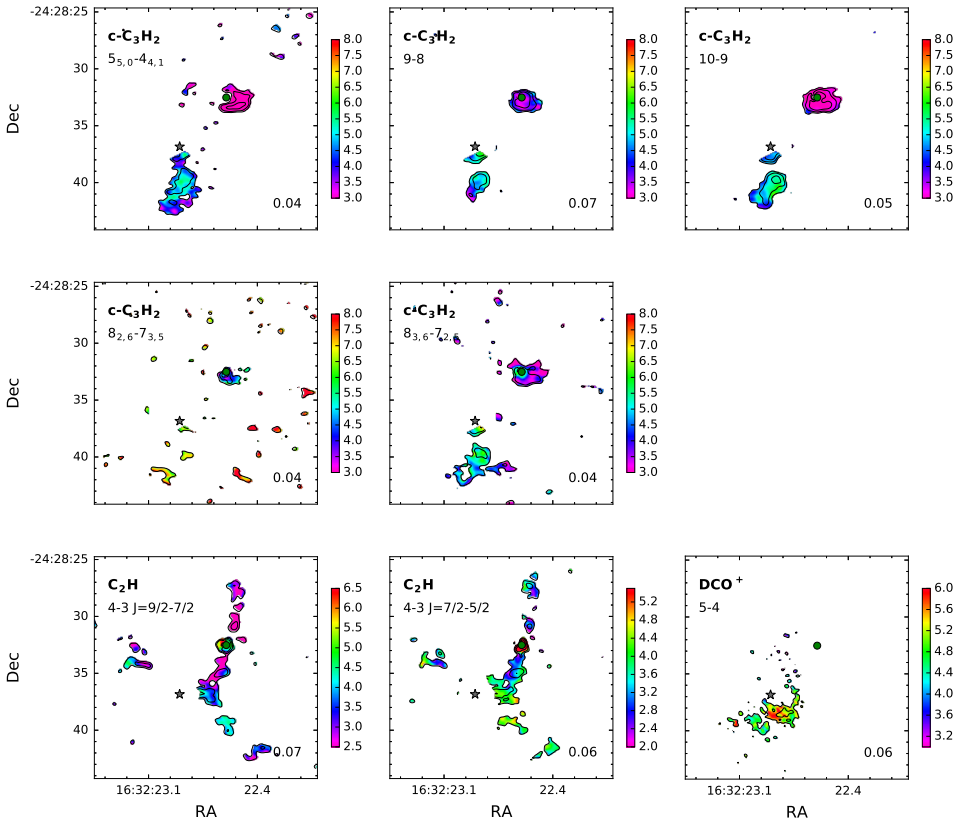

Figure 11: Intensity (contours) and velocity (color-scale) integrated maps of c−C_3H_2, C_2H and DCO^+ towards IRAS 16293-2422. The color-bar shows the velocity range in km s^{-1} for each panel. Contours show the respective line in steps of 2, 3, 5, 20, 60 and 80σ, with σ (Jy $beam^{-1}$ km s^{-1}) indicated in the lower right corner of each panel. The postions of IRAS 16293-2422 A and B are indicated with a star and circle, respectively.

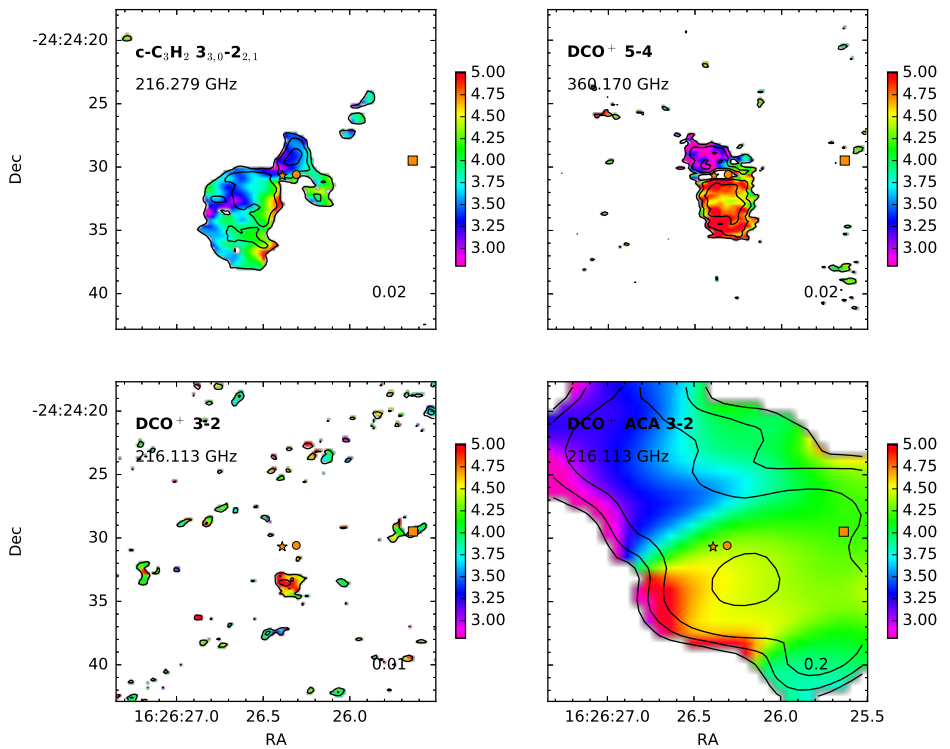

Figure 12: Intensity (contours) and velocity (color-scale) integrated maps of c$-C_3H_2$ and DCO^+ towards VLA 1623-2417. The color-bar shows the velocity range in km s^{-1} for each panel. Contours show the respective lines in steps of 2, 3, 5, 15, 20 and 30σ, with σ (Jy $beam^{-1}$ km s^{-1}) indicated in the lower right of each panel. The positions of VLA 1623-2417 A, B and W are indicated with a star, circle and square, respectively.

position of VLA. N_2D^+ also exhibits the same behaviour (Punanova et al. 2016). Furthermore, *Herschel* observations of high-J N_2H^+ towards VLA (Liseau et al. 2015; Favre et al. 2017)) show that the molecule is detected up to the J = 6–5 transition peaking at ∼0.1 K km s^{-1} but the emission is extended. The observed parameters of N_2H^+ and N_2D^+ from Punanova et al. (2016) and Favre et al. (2017) are listed in Table 7.

Using the observed transitions of N_2H^+ and N_2D^+, we derive density and excitation temperature with the method described in Sect. 4.4.1. The different beam sizes of the observations require a beam dilution correction factor that is given by $T'_{\rm mb} = T_{\rm mb,obs} \frac{\theta^2_{\rm source}}{\theta^2_{\rm source}+\theta^2_{\rm beam}}$, where $T'_{\rm mb}$ and $T_{\rm mb,obs}$ are the corrected and observed main beam temperature, respectively, $\Omega_{\rm beam}$ is the solid angle of the single-dish beam and $\Omega_{\rm source}$ is the solid angle subtended by the source. We assume the emission is concentrated in the region of the smaller beam, which would be of 26.5″ for N_2H^+ and 16.3″ for N_2D^+.

To compare with our ALMA observations, the expected peak for N_2H^+ 4–3 and N_2D^+ 3–2 is derived from the observations of Punanova et al. (2016) and Favre et al. (2017). The N_2H^+ molecular data file without hyperfine structure is used to calculate the kinetic temperature of both molecules. Since LAMDA does not have a molecular data file for N_2D^+, the data file for N_2H^+ is used, selecting the corresponding transition rather than frequency. For the predicted peak emissions for N_2H^+ 4–3 and N_2D^+ 3–2, two cases are examined: i) the observed emission is evenly distributed in the single-dish beam (i.e., beam filling factor = 1) and ii) the emission is concentrated in a 1″ region (i.e. beam filling factor < 1). The second case introduces a beam dilution correction. The results of the calculation are listed in Table 7.

The kinetic temperature and number density obtained in our calculations (∼11 K, $\sim10^{7-9}$ cm^{-3}) are slightly higher than those previously reported (7.7 K, 10^6 cm^{-3}; Punanova et al. 2016). The column densities, however, are similar to those reported in Punanova et al. (2016). For N_2H^+, our results are also consistent with those reported in Liseau et al. (2015).

Using the physical parameters obtained from the DCO^+ 5–4/3–2 ratio (Sect. 4.4.1 and Table 4), we calculate a column density of 1.5–2×10^{13} cm^{-2} for N_2D^+. If instead we use the physical parameters obtained from the N_2D^+ observations towards VLA, we find a column density of 4–5×10^{13} cm^{-2} for N_2D^+ 3–2 towards IRAS. For both sets of parameters, the column density is higher by one order of magnitude in comparison to the N_2D^+ toward VLA.

4.C PILS full spectra

The PILS survey spectra (Jørgensen et al. 2016) is reproduced here for the south c−C_3H_2 peak position and at one beam away from the position of IRAS-B. Figures 13, 14 and 15 present the full spectra for both positions. At the south c−C_3H_2 peak position, the spectra is multiplied by a factor of 10 to bring out the features. Few molecular lines are detected at this position, apart from common molecules like HCO^+ and CO, only c−C_3H_2 and H_2CS are detected.

Table 6: c−C_3H_2 and C_2H peak intensities.

Molecules	c−C_3H_2					C_2H			
Transition	5–4	9–8	10–9	8–7	8–7	J=9/2–7/2 F=5–4	J=9/2–7/2 F=4–3	J=7/2–5/2 F=4–3	J=7/2–5/2 F=3–2
IRAS 16293-2422 (rms = 10 mJy beam^{-1})									
South	240	410	350	90	200	≤20	30	10	20
Centre	40	30	30	20	30	170	140	140	110
North	30	50	40	20	20	150	130	110	110
VLA 1623-2417 - APEX (rms = 80 mK)									
A	...	...	...	...	...	960	616	680	342

Table 7: N_2H^+ and N_2D^+ parameters for VLA 1623-2417.

	Observed			
Parameter	N_2H^+ 1–0[a]	N_2H^+ 6–5[b]	N_2D^+ 1–0[a]	N_2D^+ 2–1[a]
$T_{\rm mb}$ (K)	3.3 ± 0.1	0.2 ± 0.1	0.57 ± 0.1	1.5 ± 0.2
$\Delta v_{\rm SD}$ (km s^{-1})	0.56 ± 0.01	0.7 ± 0.2	0.55 ± 0.03	0.55 ± 0.01
$\eta_{\rm mb}$	0.95	0.63	0.95	0.94
$\Omega_{\rm beam}$ ($''$)	26.5	36	32.1	16.3
Ratio	0.06 ± 0.03		2.6 ± 0.6	
Col. density (cm^{-2})	1.3×10^{13}		1.8×10^{12}	
H_2 density (cm^{-3})	5×10^7 – 7×10^9		5×10^7 – 7×10^9	
$T_{\rm ex}$ (K)	11 – 12		11 – 12	
$\Omega_{\rm source} = \Omega_{\rm beam}$	N_2H^+ 4–3		N_2D^+ 3–2	
$S_{\rm pred}$ (mJy beam^{-1})	99		22	
$\Omega_{\rm beam,obs}$ ($''$)	0.85		0.76	
$\sigma_{\rm obs}$ (mJy beam^{-1})	94.9		8.58	
S/N	1		2.6	
$\Omega_{\rm source} = 1''$	N_2H^+ 4–3		N_2D^+ 3–2	
$S_{\rm pred}$ (mJy beam^{-1})	2631		364	
$\Omega_{\rm beam,obs}$ ($''$)	0.85		0.76	
$\sigma_{\rm obs}$ (mJy beam^{-1})	94.9		8.58	
S/N	27		42	

Notes. [a] IRAM 30m observations from Punanova et al. (2016). [b] *Herschel* observations from Favre et al. (2017)

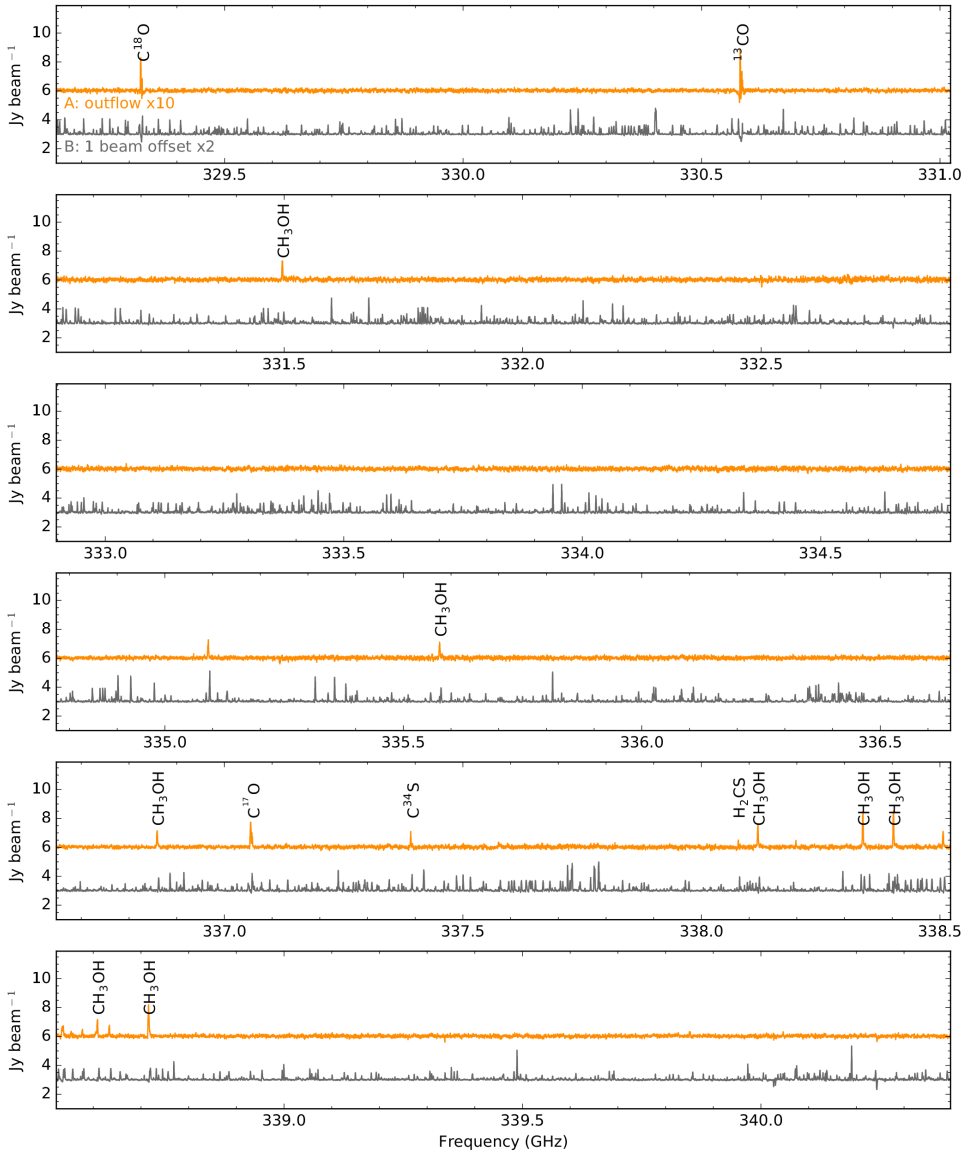

Figure 13: Full spectra obtained in the PILS survey for IRAS 16293-2422. Here the frequency range 329.15 to 340.4 GHz is shown. The rest of the spectra is shown in Fig. 14 and 15. The spectra for the IRAS 16293-2422 B is one beam away from the source position, note that it is multiplied by a factor of 2. The spectra for IRAS 16293-2422 A's outflow is centered at the observed peak of c$-C_3H_2$, note that it is multiplied by a factor of 10 and shows very little emission other than c$-C_3H_2$, CH_3OH, H_2CS, H_2CO and HCO^+.

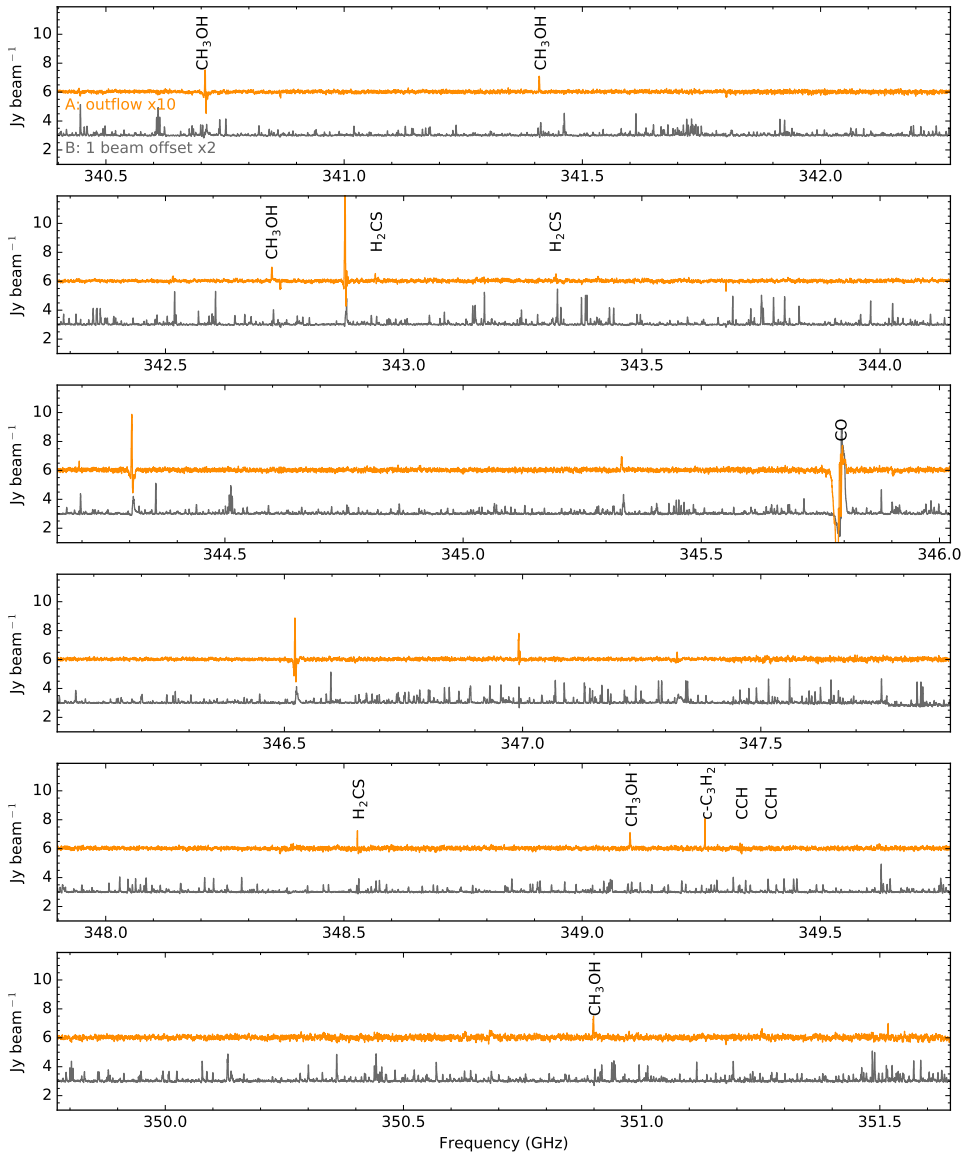

Figure 14: Same as in Fig. 13 but for the frequency range 340.4 to 351.65 GHz. C_2H is marked for reference.

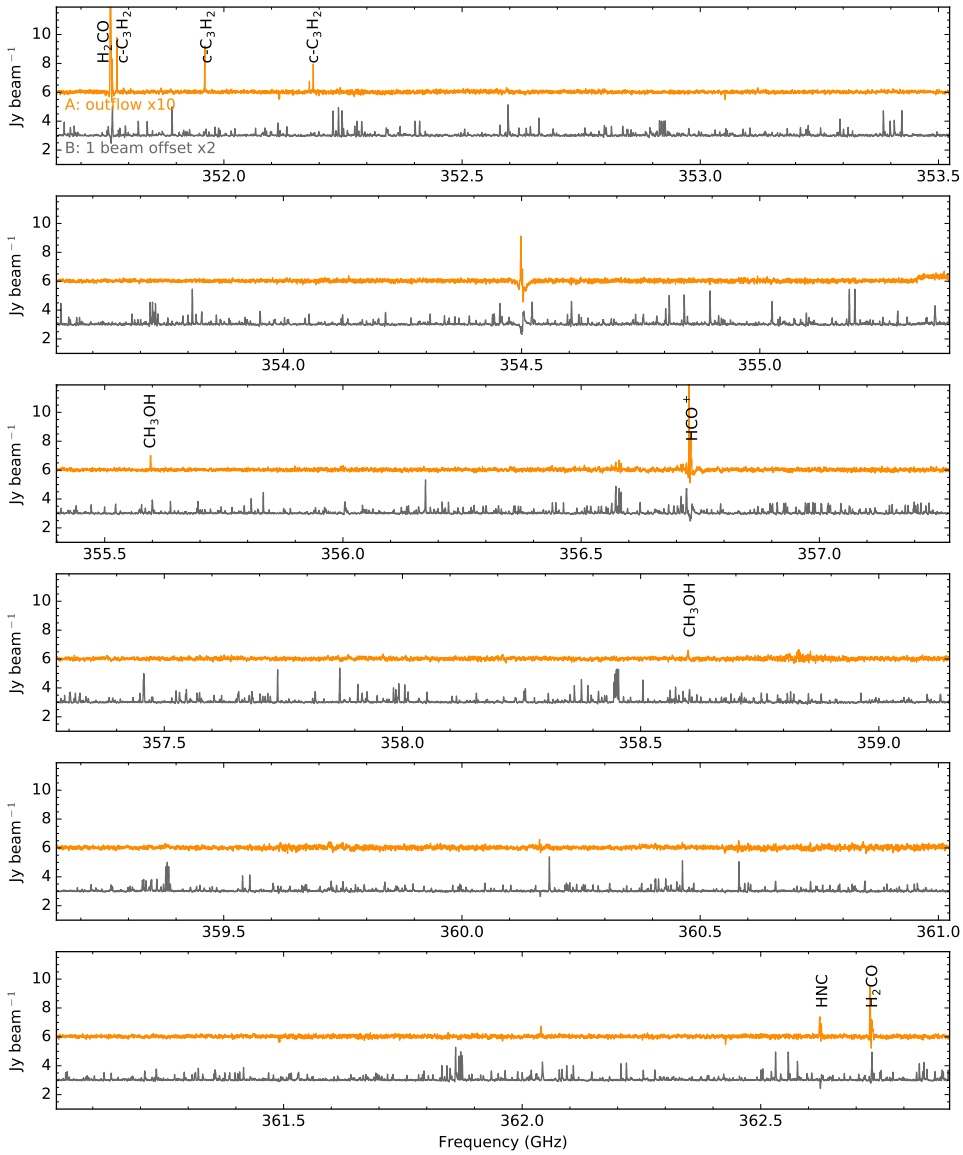

Figure 15: Same as in Fig. 13 but for the frequency range 351.65 to 362.9 GHz.